DEPARTMENT OF PHYSICS
UNIVERSITY OF JYVÄSKYLÄ
RESEARCH REPORT No. 9/2010

ANALYSIS OF FLUID FLOW THROUGH POROUS MEDIA BASED ON X-RAY MICRO-TOMOGRAPHIC RECONSTRUCTIONS

BY
VIIVI KOIVU

Academic Dissertation
for the Degree of
Doctor of Philosophy

To be presented, by permission of the
Faculty of Mathematics and Science
of the University of Jyväskylä,
for public examination in the old grand hall (S212) of the
University of Jyväskylä on 22nd October 2010
at 12 o'clock

Jyväskylä, Finland
October, 2010

To my children

Preface

The work reviewed in this thesis has been carried out during the years 2005-2010 in the Department of Physics at the University of Jyväskylä. The financial support from the Finnish Graduate School in the Material Physics, University of Jyväskylä and Metso Paper Oy is gratefully acknowledged.

I would like to thank Professor Markku Kataja and Professor Jussi Timonen for their guidance during these years and for the possibility to work in their group. Especially I want to express my gratitude to my supervisor Markku Kataja for his valuable contribution during preparation of the manuscript of this thesis.

I am grateful to my father Sakari Villa and school science teachers Seppo Bütt and Matti Perho for paving (and occasionally enforcing) me to the way of science. I would like to thank Marko Rasi, Esa Rehn and Kimmo Ranttila for technical support in the beginning of my Ph.D. studies, Risto Talja and Petter Honkalampi for interesting project management, Rodrigo Robinson for teaching me some mysteries of chemistry, Jari Hyväluoma for scientific guidance, Arttu Miettinen for helping me with image analysis, Jarno Alaraudanjoki for technical and scientific support, Sabine Rolland du Roscoat for helping me with sychrotron -based x-ray tomography imaging, and Professor Christian Geindreau and Professor Jean-Francis Bloch for their contribution to two of the enclosed articles. Words cannot express the appreciation and thankfulness for my dear friends Keijo Mattila, Antti Nuottajärvi, Hannu Koivisto, Rauni Seppänen and Tuomas Turpeinen for scientific help and support, but also strong and close friendship during these years. I feel privileged to have friends like you.

Finally, I thank my parents Eija and Sakari and the whole family Mannonen for being the tower of strength to me during my entire life. I express my gratitude to my brother Visa and his common-law wife Tiina for support and company. I thank my dear little daughter Julia for all the joy and love she gives me every single day. Most of all, I would like to thank my beloved husband Jari for love, encouragement and patience in the past, today and tomorrow.

Jyväskylä, October 2010

Viivi Koivu

Abstract

Koivu, Viivi
Analysis of fluid flow through porous media based on x-ray micro-tomographic reconstructions
Jyväskylä: University of Jyväskylä, 2010, 158 p.
(Research report/Department of Physics, University of Jyväskylä,
ISSN 0075-465X; 9/2010)
ISBN 978-951-39-4032-4
diss.

This thesis deals with creeping fluid flow through fibrous porous materials. Permeability through a porous medium is a measure of the ability of the material to transmit fluids. For testing and demonstration purposes the permeability values of a few fibrous heterogeneous materials, namely synthetic non-woven felt, wet pressing felt, cardboard, newsprint and hardwood paper, were measured experimentally. Reconstructions of the same materials under similar compression states were captured by x-ray micro-tomography. The actual microscopic pore structure thus obtained was utilised in the numerical lattice-Boltzmann analysis for solving the fluid flow permeability of the materials. Agreement between the experimental and numerical results was good. In addition, numerical permeability results for certain geometries were compared to the values obtained by finite-difference and finite-element methods. All numerical results were found to be in close agreement. The resolution of the tomographic reconstructions is limited causing discretisation uncertainty in the numerical analysis. The reliability of the numerical results was estimated by performing simulations for high and low resolution lattices. These results were further compared to the corresponding analytical solutions. The discretisation uncertainty was found not to be essentially larger than the typical total uncertainty of the experimental results. The advantage of the combination of x-ray tomography and numerical methods arises in the cases where direct experimental measurements are not feasible. An example of such an application, reported in this thesis, is to analyse the permeability of individual, distinct layers in a layer-structured material in order to determine the contribution of this layer to the overall permeability.

In the final part of the work, tomographic reconstructions of porous heterogeneous materials were combined to a void space segmentation analysis. The utilisation of the method was demonstrated by running the analyses for a series of tomo-

graphic reconstructions of liquid packaging boards. The methods facilitate e.g. the analysis between the structural characteristics of pore structure and their relation to imbibition process. Demonstration analyses indicate the void space segmentation analysis to give valuable information on correlations between the structure of porous heterogeneous materials and their fluid flow properties.

Keywords Single phase fluid flow, compressible porous media, permeability, imbibition, lattice Boltzmann method, x-ray micro-tomography, pore structure

Author's address Viivi Koivu
Department of Physics
University of Jyväskylä
Finland

Supervisor Professor Markku Kataja
Department of Physics
University of Jyväskylä
Finland

Reviewers Dr. Hannes Vomhoff
INNVENTIA AB
Stockholm
Sweden

Professor Jouni Paltakari
Department of Forest Products Technology
Helsinki University of Technology
Finland

Opponent Professor Steven Keller
Department of Paper and Chemical Engineering
University of Miami
United States of America

List of Publications

Appendix I KOIVU V., MATTILA K. AND KATAJA M., *A method for measuring Darcian flow permeability*. Nordic Pulp Paper Res. J. **24(4)** (2009) 395–402.

Appendix II KOIVU V., DECAIN M., GEINDREAU C., MATTILA K., ALARAUDANJOKI J., BLOCH J.-F. AND KATAJA M., *Flow permeability of fibrous porous materials. Micro-tomography and numerical simulations*. 14th Fundamental Research Symposium, Oxford, September (2009) 437–454.

Appendix III KOIVU V., DECAIN M., GEINDREAU C., MATTILA K., J., BLOCH J.-F. AND KATAJA M., *Transport properties of heterogeneous materials. Combining computerised X-ray micro-tomography and direct numerical simulations*. Int. J. Comp. Fluid Dynamics **23(10)** (2010) 713–721.

Appendix IV KOIVU V., SEPPÄNEN R., TURPEINEN T., MATTILA K., HYVÄLUOMA J. AND KATAJA M., *Combining X-ray micro-tomography and image analysis to study imbibition and void space in liquid packaging board*. J. Pulp Paper Sci., accepted for publication

The author of this thesis has been involved in the design, testing and operation of the experimental equipment, and in the analysis of the collected data. The majority of the results presented in this thesis are reported in the enclosed articles in Appendices I-IV. The author of this thesis has performed the experimental measurements, x-ray tomographic imagings and the numerical lattice Boltzmann analyses reported. She has also written the largest part of the enclosed articles.

In Appendix I, the experimental permeability measurement procedure is introduced and the experimental permeability values are compared to the numerical lattice-Boltzmann results. Appendix II represents a special application of the combination of x-ray micro-tomographic reconstructions and numerical analysis. Uncertainty of the numerical analysis results is estimated in Appendix III. Appendix IV provides new perspectives for porous materials research combining x-ray micro-tomography and image analysis.

Nomenclature

a	capillary radius [m]
A	cross sectional flow area [m^2]
A_p	cross sectional area of pore channel [m^2]
A_{eff}	effective flow area [m^2]
A_0	area of permeable central region [m^2]
c	constant in Kozeny-Carman equation [dimensionless]
C	water absorption coefficient [$kg/(m^2 s^{1/2})$]
δC_A	uncertainty of flow area [m^2]
$\delta C_{L_{ii}}$	uncertainty of sample thickness [m]
δC_P	uncertainty of pressure loss [Pa]
$\mathbf{f}$	body force [$kg/(m^2 s^2)$]
$\mathbf{g}$	gravitation vector [m/s^2]
h	height of liquid column in capillary [m]
H	average height of liquid column [m]
J	constant in Drummont and Tahir equation [dimensionless]
k	permeability coefficient [m^2]
$k_\perp$	permeability coefficient for flow perpendicular to cylindrical rods [m^2]
$k_\parallel$	permeability coefficient for flow parallel to cylindrical rods [m^2]
k_{ii}	diagonal component of permeability tensor [m^2]
K	constant in Drummont and Tahir equation [dimensionless]
l_p	perimeter of pore channel [m]
L	characteristic length scale [m]
L_e	average length of tortuous flow paths [m]
L_i	thickness of sample (at state i), distance between two ends of capillary [m]
L_0	thickness of sample at reference state [m]
m_1	constant in Brundrett equation [dimensionless]
m_2	constant in Brundrett equation [m^2]
M	mass of imbibibed liquid [g]
p	pressure [Pa]
ΔP	pressure drop [Pa]
P_{ave}	average pressure [Pa]
P_{in}	pressure at inlet [Pa]
P_{out}	pressure at outlet [Pa]

$\mathbf{q}$	superficial volume flux [m/s]
q_i	volume flux in i-direction [m/s]
Q	volumetric flow rate [m^3/s]
r	cylinder radius [m]
r_{eff}	effective pore radius [m]
r_h	mean hydraulic radius [m]
Re	Reynolds number [dimensionless]
S_0	specific surface area [m]
t	time [s]
$\mathbf{u}$	velocity [m/s]
V	characteristic velocity scale [m/s]
W	grammage [g/m^2]
Z	coordination number [dimensionless]

Greek symbols

γ	surface tension [kg/s^2]
θ	contact angle [degree]
$\boldsymbol{\kappa}$	permeability tensor [m^2]
μ	dynamic viscosity [(kg m)/s]
ρ	density [kg/m^3]
τ	tortuosity [dimensionless]
ϕ	porosity [%]
ϕ_0	porosity of sample at reference state [%]
ϕ_s	solid volume fraction [%]
Ψ	pietsometric head [Pa]

Contents

Chapter 1

Introduction

Heterogeneous materials in the most general sense are composed of domains of different materials or the same material in different states. For instance foams, composite materials, concrete, paper, cardboard, textile felt, bone, sandstone, soils and sea ice are very common examples of man-made and natural heterogeneous materials [Bear, 1972, Adler, 1992, Torquato, 2001]. Fluid flow phenomena in porous heterogeneous materials can be found in many important processes in nature and in society. In particular, fluid flow through a porous medium contribute to several technological problems, e.g. extraction of oil or gas from porous rocks, spreading of contaminants in fluid-saturated soils and certain separation processes, such as filtration [Torquato, 2001]. In paper industry single and multi phase fluid flow properties in porous media play important roles related to manufacturing process and product development.

The general laws describing creeping fluid flows are well known. However, a detailed study of fluid flow in porous heterogeneous media is complicated. This is a direct consequence of the often very complex, internal micro-scale structures of these materials. That is, the interplay between fluid flow and complex internal structure at the micro-scale gives rise to the effective fluid flow properties at the macro-scale. The details of the internal micro-scale structures of various materials can be revealed by utilising computerised x-ray micro-tomography [Coles et al., 1998, Samuelsen et al., 2001, Goel et al., 2001, Thibault and Bloch, 2002, Holmstad et al., 2003, Rolland du Roscoat et al., 2005, Goel et al., 2006, Stock, 2009]. X-ray tomography is a noninvasive and nondestructive imaging method where individual x-ray images recorded from different viewing directions are used for reconstructing the internal 3D structure of the object of interest [Stock, 2009]. During the recent decade, the precision of x-ray tomographic imaging techniques have reached the sub-micrometre resolution and enables analyses of statistical properties of various materials. Combined to numerical analysis the tomographic reconstructions facilitate analyses of the effective material properties of realistic porous media [Manwart et al., 2002, Thibault and Bloch, 2002, Aaltosalmi et al., 2004, Ramaswamy et al.,

2004,Rolland du Roscoat et al., 2005,Kutay et al., 2006,Hyväluoma et al., 2006,Fourie et al., 2007].

In various industrial and scientific applications an effective material property, permeability, is used for describing the ability of porous materials to transmit fluids. Permeability coefficient for single phase creeping fluid flow through a porous media is defined by the phenomenological law by Henry Darcy as the a proportionality constant between the average fluid velocity and applied pressure gradient [Darcy, 1856].

Permeability of various porous media has been studied analytically, numerically and experimentally by many researchers [Darcy, 1856, Happel, 1959, Chen, 1982, Drummont and Tahir, 1984, Jackson and James, 1986, Succi et al., 1989, Brundrett, 1993, Boerner and Orloff, 1994, Vomhoff, 1998, Vomhoff et al., 2000, Pan et al., 2006, White et al., 2006, Vidal et al., 2008, Thibault and Bloch, 2008]. The analytical approaches are often confined to simplified sample geometries. Some of the numerical studies are based on analysis made for computationally generated models of porous media [Rasi et al., 1999, Aaltosalmi et al., 2004, Belov et al., 2004, Lundström et al., 2004, Verleye et al., 2005, Verleye et al., 2007]. Tomographic reconstructions are increasingly utilised in combination with numerical methods to analyse permeability of porous heterogeneous materials [Manwart et al., 2002, Martys and Hagedorn, 2002, Aaltosalmi et al., 2004, Kutay et al., 2006, Fourie et al., 2007]. Some of the experimental methods are applicable only for measuring permeability of bulky rigid samples [Saar and Manga, 1999, Abraham et al., 2000, Loosveld et al., 2002, Schlup et al., 2002]. However, various challenges have arisen in measuring permeability of soft thin sheet-like samples, such as paper and cardboard, under mechanical compression. The transverse flow measurement involves compressing the sample between perforated or porous plates and inducing fluid flow through the plates and the sample. The basic difficulty in such a measurement lies in even application of mechanical load while maintaining undisturbed and controlled flow through the sample. This is due to the reason that, the perforated porous plates have to be open for fluid flow and at the same time solid and planar to supply mechanical load evenly over the entire sample area. For the in-plane flow measurement the difficulties arise from narrow flow area due to planar profiles of the samples or difficulties in sample preparation. For both the transverse and in-plane permeability measurements, misinterpretation of data can be caused by accumulated compression of soft porous material in flow direction or leakages bypassing the sample.

The main objective of this thesis was to develop procedures for analysing fluid flow permeability of soft porous sheet-like materials. The underlying motivation for this was to find out if it is possible to numerically model fluid flow in realistic porous materials and to obtain results that agree quantitatively with experimental data. The permeability coefficients were here analysed in two ways: on the one hand, by using the numerical lattice Boltzmann method in combination with to-

mographic reconstructions of the materials and, on the other hand, experimentally by permeability measurement device. The three-dimensional structures of selected samples were obtained by utilising x-ray tomography. These reconstructions were further used as simulation geometries for numerical fluid flow analysis. Before numerical analysis it is usually necessary to process the tomographic reconstructions in various ways. All these steps may contribute to the final results of the numerical analyses. Special attention was paid to the tomographic sample preparation and image processing in order to produce as realistic simulation geometries as possible. The resolution of tomographic reconstructions is limited causing uncertainty for the numerical results. This effect was also evaluated. The experimental method reported in this thesis is especially designed for measuring thin sample sheets. The construction of the permeability measurement apparatus, the experimental procedure and the data processing were all designed and manufactured in the purpose of minimising the known sources of uncertainty. The device was applied here for measuring the transverse and in-plane flow permeability of the selected samples.

Generally, the fluid flow during permeability measurement is driven by external body force or pressure difference and the pore space of the medium is assumed to be fully saturated. Another flow phenomenon considered in this thesis is spontaneous imbibition process, where one fluid is displaced by another immiscible fluid. Spontaneous flow of wetting fluids in porous media is often described by capillary laws. The law of imbibition is often attributed to Lucas and Washburn [Lucas, 1918, Washburn, 1921a, Washburn, 1921b]. Methods combining tomographic reconstructions and advanced image analysis to study connections between structure of void space and imbibition in porous heterogeneous materials are reported. This work combines the experimental, image processing, and numerical methods to provide new insight into fluid flow properties of porous heterogeneous materials.

The outline of this thesis is as follows. In Chapter 2, the basic concepts and flow relations for fluid transport in porous media are provided. In Chapter 3, the experimental permeability measurement device and measurement procedures are presented. Chapter 4 focuses on the numerical lattice Boltzmann permeability analysis and application of tomographic reconstructions for the simulations. Comparison of the numerical and experimental methods is discussed in this chapter. Chapter 5 concentrates on applications of the experimental and numerical methods for studying permeability values of various porous heterogeneous materials. In Chapter 6, imbibition and structural properties in porous heterogeneous materials are studied. In the final chapter, Conclusion and Outlook, the work is summarised and concluded.

Chapter 2

Fluid flow properties in porous materials

Fluid flow in a porous medium can be driven by e.g. external body force, pressure gradient or capillary forces. The motion of incompressible Newtonian fluid in microscopic level is described by the basic hydrodynamical flow equations, the continuity equation

$$\nabla \cdot \mathbf{u} = 0, \tag{2.1}$$

and the momentum equation (Navier-Stokes eq.)

$$\rho \left(\frac{\partial \mathbf{u}}{\partial t} + \mathbf{u} \cdot \nabla \mathbf{u} \right) = -\nabla p + \mu \nabla^2 \mathbf{u} + \mathbf{f}, \tag{2.2}$$

where ρ is the density of the fluid, $\mathbf{u}$ is the velocity of the fluid, t is time, ∇ is the gradient operator, p is the pressure of the fluid, μ is the dynamic viscosity of the fluid and $\mathbf{f}$ represents forces per unit volume acting on the fluid (body force) [White, 2003, Adler, 1992]. The continuity equation is a mathematical statement for the rate at which mass enters a system is equal to the rate at which mass leaves the system. Momentum equation relates the sum of the forces acting on an element of fluid to its acceleration or rate of change of momentum.

The ratio between the inertial and viscous forces is given by the Reynolds number:

$$Re = \frac{\rho V L}{\mu}, \tag{2.3}$$

where V and L are the characteristic velocity and length scale of the fluid flow, respectively. At small Reynolds number inertial forces are small in comparison to the viscous forces, and the left hand side of Eq. (2.2) becomes negligible. Thus Eq. (2.2) reduces to the Stokes equation:

$$\nabla p = \mu \nabla^2 \mathbf{u} + \mathbf{f}. \tag{2.4}$$

For thermal flows, one needs in addition an energy equation. In this thesis, isothermal flows of Newtonian fluids are considered, and hence the energy equation is not needed.

Equations (2.1-2.4) are valid on the microscopic (pore-scale) level. Fluid flow on macroscopic level is often described by effective laws discussed in the next section.

2.1 Permeability

Darcy's law

With low values of Reynolds number, an incompressible steady-state isothermal Newtonian fluid flow in porous materials is governed by the phenomenological Darcy's law [Darcy, 1856, Bear, 1972, Dullien, 1979, Adler, 1992]

$$\mathbf{q} = \frac{-\boldsymbol{\kappa}}{\mu} \cdot \nabla \Psi, \tag{2.5}$$

where $\mathbf{q}$ is the superficial volume flux and $\boldsymbol{\kappa}$ is the permeability tensor. The pietsometric head Ψ is defined by $\nabla\Psi = \nabla p - \rho\mathbf{g}$, where p is the pressure, ρ is the density of the fluid and $\mathbf{g}$ is the acceleration due to body force (gravity), see Fig 2.1. In general, permeability is a symmetric second-order tensor [Liakopoulos, 1965]:

$$\boldsymbol{\kappa} = \begin{bmatrix} k_{xx} & k_{xy} & k_{xz} \\ k_{yx} & k_{yy} & k_{yz} \\ k_{zx} & k_{zy} & k_{zz} \end{bmatrix}. \tag{2.6}$$

In this thesis, the diagonal values of the permeability tensor in a case dependent coordinate system are found experimentally by the integrated form of Darcy's law

$$k_{ii} = -\frac{\mu q_i}{\Delta P/\Delta L_i} = -\frac{\mu Q_i \Delta L_i}{A(P_{out} - P_{in})}, \tag{2.7}$$

where Q is the volumetric flow rate through the sample, A is the cross-sectional flow area, $\Delta P = P_{out} - P_{in}$ is the pressure drop and ΔL_i is the length over which the pressure drop takes place. Figure 2.1 shows a schematic illustration of a case where fluid flow (in negative z direction) occurs through a porous sample.

Equation (2.7) is valid for the incompressible fluid flows. For gas flows through porous medium Darcy's law must be slightly modified to account for compressibility effects. For isothermal compressible flow the permeability coefficient is thus given by

$$k_{ii} = -\frac{\mu q_i}{\Delta P/\Delta L_i}\frac{P_{out}}{P_{ave}} = -\frac{\mu Q \Delta L_i}{A(P_{out} - P_{in})}\frac{P_{out}}{P_{ave}}, \tag{2.8}$$

where P_{out} is the pressure, Q is the volumetric flow rate at the downstream side of

the medium, and $P_{ave} = P_{out} + \frac{1}{2}(P_{in} - P_{out})$ is the average pressure [Bear, 1972, Leskelä and Simula, 1998].

Although the permeability is generally perceived as a property of porous material itself, various authors report higher values of permeability coefficient for gas flow than for liquid flow through the same porous medium, see e.g. Refs [Klinkenberg, 1941, Bear, 1972, Wu et al., 1998, Tanikawa and Shimamoto, 2006]. Possible interactions between liquid and a porous material (e.g. swelling) can generate changes in the pore structure and therefore cause difference between the results for gas and liquid measurements. Also deviation from Darcy's law occur e.g. at high flow rates and with gas flows at low pressures.

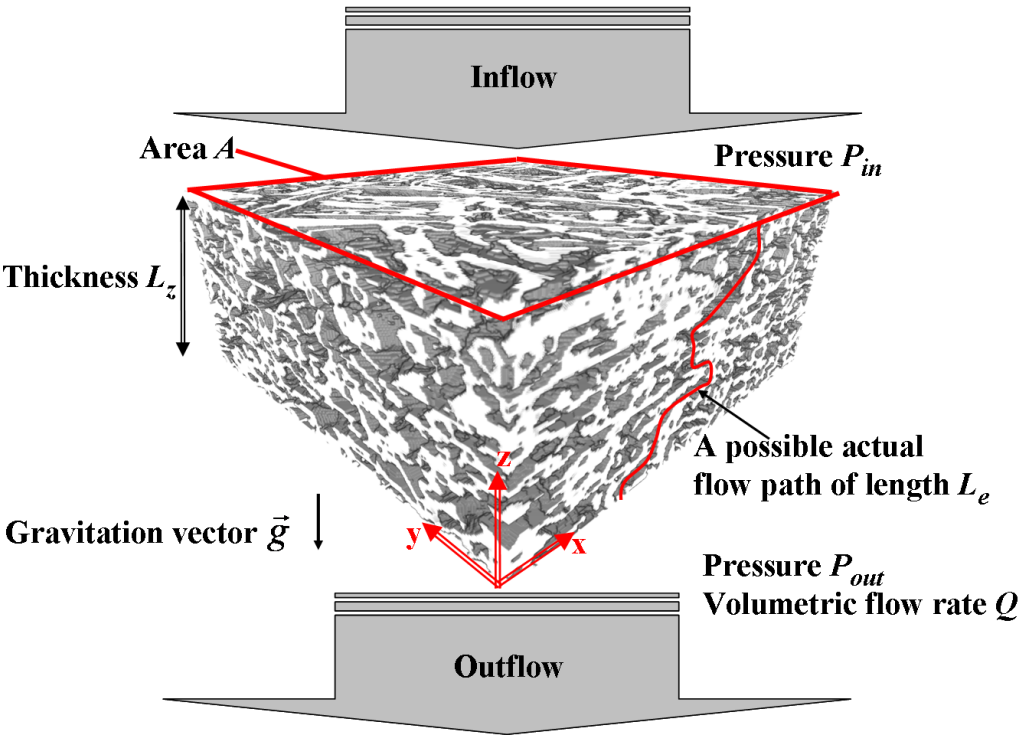

FIGURE 2.1 A schematic illustration of fluid flow through a porous material.

Permeability models

Several theoretical results for permeability coefficients have been reported in the literature. Perhaps the most common formula which can be derived analytically for simplified capillary model is the Kozeny-Carman relation

$$k = \frac{1}{c}\tau^2 {S_0}^2 \frac{\phi^3}{(1-\phi)^2}, \tag{2.9}$$

where c is a constant that depends on the cross section of the capillaries (being $c = 2$ for circular cross section), S_0 is the specific surface area, τ is the tortuosity of the flow and ϕ is the porosity of the media [Bear, 1972, Dullien, 1979]. The tortuosity is defined by equation

$$\tau = (L_e)^2/(L_i)^2, \tag{2.10}$$

where L_e is the length of the flow path through a tortuous capillary tube and L_i is the length of a straight line connecting the two ends of the tube. For realistic porous materials, tortuosity can be estimated by replacing L_e by average length of tortuous flow paths through a porous medium and L_i by the thickness of the medium, see Fig. 2.1.

Several analytical permeability results have been derived especially for fibrous porous materials modeled as an array of cylindrical rods. Examples of those are the formulas derived by Happel [1959], by Kuwabara [1959] and by Drummont and Tahir [1984] for fluid flow perpendicular to an array of rods:

$$\frac{k_\perp}{r^2} = \frac{1}{8\phi_s}\left(-\ln\phi_s + \frac{\phi_s^2-1}{\phi_s^2+1}\right) \quad \text{(Happel)} \tag{2.11}$$

$$\frac{k_\perp}{r^2} = \frac{1}{8\phi_s}\left(-\ln\phi_s - \frac{3}{2} + 2\phi_s\right) \quad \text{(Kuwabara)} \tag{2.12}$$

$$\frac{k_\perp}{r^2} = \frac{1}{8\phi_s}\left(-\ln\phi_s - K + 2\phi_s - J{\phi_s}^2\right) \quad \text{(Drummont and Tahir)} \tag{2.13}$$

where $\phi_s = 1 - \phi$ is the volume fraction of solids and r is the radius of the cylinders. Equations (2.11) and (2.12) were derived for flow past an array of randomly placed parallel cylinders. In Eq. (2.13), K and J are constants that depend on the arrangement of the cylinders, having values $K = 1.476$ and $J = 1.774$ for square array, and $K = 1.498$ and $J = 0.5$ for hexagonal array. Sangani and Acrivos [1982] used a unit cell approach to find an exact solution for flow perpendicular to the square and hexagonal arrays of cylinders. Their solutions were given in terms of series expansions where the effect of boundary conditions must be found numerically. This result can not be expressed in closed form, but Sangani and Acrivos provided tabulated numerical results that can be applied in practical flow problems. For flow parallel to an array of cylinders, examples of approximative formulas for permeability derived

by Happel [1959] and by Drummont and Tahir [1984] are:

$$\frac{k_{\parallel}}{r^2} = \frac{1}{4\phi_s}\left(-\ln\phi_s - \frac{3}{2} + 2\phi_s - \frac{1}{2}{\phi_s}^2\right) \quad \text{(Happel)} \tag{2.14}$$

$$\frac{k_{\parallel}}{r^2} = \frac{1}{4\phi_s}\left(-\ln\phi_s - K + 2\phi_s - \frac{1}{2}{\phi_s}^2\right) \quad \text{(Drummont and Tahir)} \tag{2.15}$$

In Eq. (2.15) the constant K has the same values as in Eq. (2.13) for square and hexagonal arrays. Permeability of randomly oriented rods in 3D was derived by Jackson and James [1986]:

$$\frac{k}{r^2} = \frac{3}{20\phi_s}\left(-\ln\phi_s - 0.931\right) \quad \text{(Jackson and James)} \tag{2.16}$$

which is a weighted average of the permeabilities for flow parallel and perpendicular to a bundle of cylinders. All these equations, Eqs (2.11)-(2.16) are applicable for homogeneous bulk material well away from its boundaries. Another extremity is very thin sample sheets, which can be considered as gauzes. Several equations have been derived for predicting pressure loss caused by thin screens or gauzes, see e.g. Refs [Weighart, 1952, Annand, 1952, Grootenhuis, 1954, Pinker and Herbert, 1967, Brundrett, 1993]. On the creeping flow limit and by identifying the effective open area of the screen with volumetric porosity, e.g. the Brundrett law leads to the equation

$$k = m_1 \frac{\phi^2}{(1-\phi^2)}, \tag{2.17}$$

where m_1 is a constant that depends on the structure of the screen and the Reynolds number of the flow.

2.2 Imbibition

Imbibition in a porous material is defined as the displacement of one fluid by another immiscible fluid. This process is controlled and affected by a variety of factors, such as pressure gradient and capillary forces. Spontaneous imbibition in a porous material occurs when wetting liquid invades it solely under the influence of capillary forces, with no external driving pressure.

Wetting and capillary flow

Wetting behaviour is characterised by the contact angle θ at which a liquid – gas interface meets a solid surface, see Fig. 2.2. Wetting behavior depends on the properties of all three phases involved. The contact angle is determined by the interactions across the three interfaces. If the contact angle is less than 90, liquid is called wetting, and if the contact angle is greater than 90, liquid is called non-wetting.

When the lower end of a vertical capillary tube is placed in a wetting liquid

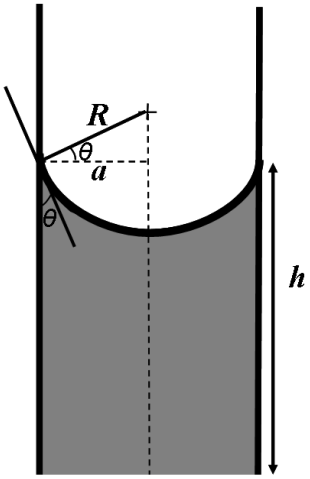

FIGURE 2.2 Capillary rise of wetting liquid in a cylindrical tube.

a concave liquid–gas surface with radius R arises. A schematic illustration of wetting liquid in a cylindrical capillary is shown in Fig. 2.2. The pressure difference Δp across the formed concave surface is

$$\Delta p = \frac{2\gamma}{R}, \tag{2.18}$$

where γ is the surface tension of the liquid [White, 2003]. The radius of the cylindrical capillary tube is a. By substituting $R = a/\cos\theta$ (see Fig. 2.2) in Eq. (2.18) the so-called Washburn equation is obtained [Washburn, 1921a]:

$$\Delta p = \frac{2\gamma\cos\theta}{a}. \tag{2.19}$$

This equation is useful for small capillaries in the cases, where gravitational effects can be neglected. Assuming fully developed Poiseuille flow, the Newton's second law for a column of wetting liquid in the capillary becomes [White, 2003]

$$\rho\left[h\frac{d^2h}{dt^2} + \left(\frac{dh}{dt}\right)^2\right] = \frac{2\gamma\cos\theta}{a} - \frac{8\mu h}{a^2}\frac{dh}{dt} - \rho g h, \tag{2.20}$$

where h is the height of the liquid column. By neglecting the inertial terms and gravity the classical Lucas and Washburn equation is obtained [Lucas, 1918, Washburn, 1921b]:

$$\frac{2\gamma\cos\theta}{a} - \frac{8\mu h}{a^2}\frac{dh}{dt} = 0. \tag{2.21}$$

The Lucas-Washburn equation describes processes where the driving capillary force is balanced by the viscous drag. Integration of equation (2.21) gives the time evolu-

tion of liquid column height:

$$h(t) = \left(\frac{a\gamma \cos\theta}{2\mu} \right)^{1/2} t^{1/2}. \tag{2.22}$$

Equation (2.22) is useful for the initial state of the imbibition experiments. It is widely used for analysing of imbibition processes in porous materials, see e.g. Refs [Bico and Quéré, 2004, Hyväluoma et al., 2006, Czél and Czigány, 2008]. However, many authors have reported deviations from the Lucas-Washburn equation for realistic porous materials [Zhmud et al., 2000, Schoelkopf et al., 2002, Alava et al., 2004, Holownia et al., 2008, Hyväluoma, 2009] and several modifications of the equation have been published [Dube et al., 2000, Schoelkopf et al., 2002, Benavente et al., 2002, Holownia et al., 2008]. These modifications typically include additional terms related to e.g. porosity ϕ of the media, roundness of the pore channels δ, tortuosity of the flow τ, pore coordination number Z (the number of neighbouring pores), the effective pore radius r_{eff} and the evaporation rate ϵ.

The void spaces of actual porous materials are highly non-trivial [Bear, 1972, Adler, 1992, Torquato, 2001] and in many cases time-dependent due to dynamic processes, e.g. swelling [Dube et al., 2000]. Complex nature of the specific internal structures of such materials induce variations e.g. in capillary pressure (see a visualisation of pore volume in a disordered fibrous sample in Fig. 2.3). Imbibition process in a porous medium depends on the physics at the pore level, i.e. at the length scales of a few micrometres or less [Dube et al., 2007]. The heterogeneity of the structure causes local and global variations in imbibition process, inducing delayed or accelerated movement of liquid front, and in consequence, imbibition roughening [Buldyrev et al., 1992, Roberts et al., 2003, Alava et al., 2004]. A visualisation of a roughened liquid front line in a porous material is shown in Fig. 2.3. This is a visualisation of one slice in a tomographic reconstruction of imbibed and freeze dried liquid packaging board sample. Potassium iodine was used in water solution to trace the imbibed liquid front in the structure. The chemical properties affecting imbibition process were found similar for the potassium iodine solution as for pure ionchanged water [Appendix IV].

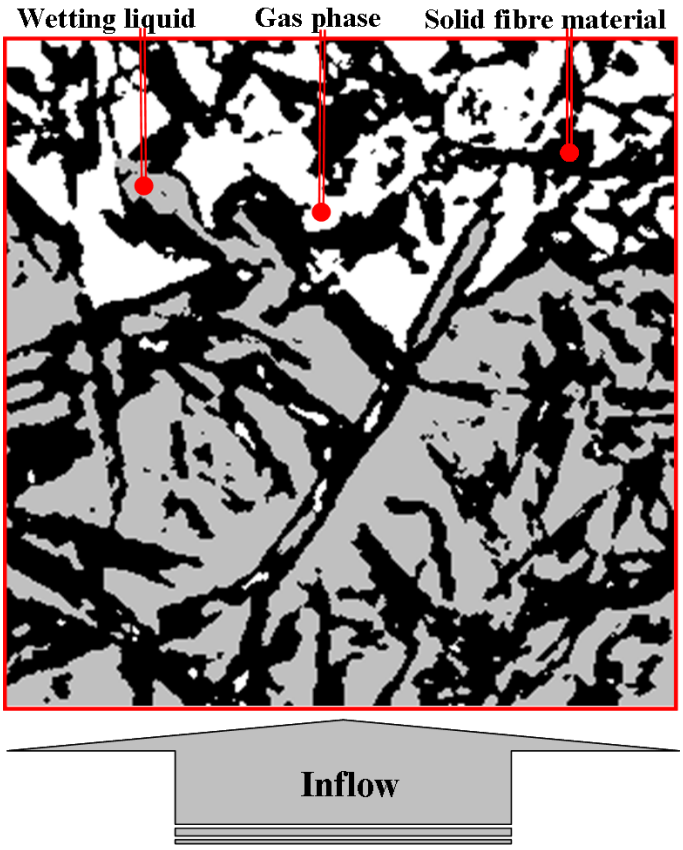

FIGURE 2.3 Visualisation of a 2D slice of a tomographic reconstruction of a liquid packaging board sample. Wetting liquid, gas phase and solid fibre material are presented by grey, white and black colours, respectively. Potassium iodine is used as contrast enhancement substance to detect the imbibing liquid front.

Chapter 3

Experimental permeability analysis

The permeability coefficients of soft fibrous porous samples have earlier been investigated by many researchers, often with applications to problems found in the paper industry, such as water removal and wet pressing, see e.g. Refs [Ceckler and Thompson, 1982, Vomhoff, 1998, Vomhoff et al., 2000, Vomhoff, 2000, Lindsay and Brady, 1993a, Lindsay and Brady, 1993b, Boerner and Orloff, 1994, Reverdy-Bruas et al., 2001, Thibault and Bloch, 2008]. For sheet-like materials, the values of permeability coefficients are typically studied for fluid flows in transverse or in-plane directions. In Fig. 2.1 with the selected coordinate conventions, the z-direction represents the transverse direction, and x and y the two perpendicular in-plane directions. Similar coordinate convention is used for all the samples discussed below.

Typically, the transverse flow measurement involves compressing the sample between perforated or porous plates and inducing fluid flow through the plates and the sample [Ceckler and Thompson, 1982, Chen, 1982, Carlsson et al., 1983, Vomhoff et al., 2000, Lindsay and Brady, 1993a, Lindsay and Brady, 1993b, Boerner and Orloff, 1994, Reverdy-Bruas et al., 2001, Thibault and Bloch, 2008]. The challenge in such a measurement, where both compression and flow take place in the direction perpendicular to the plane of the sample, lies in even application of mechanical load while maintaining undisturbed and controlled flow through the sample. Minor obliqueness or insufficient rigidity of the supporting plates and structures are likely to cause uneven macroscopic scale distribution of both load and flow through the sample. During the transverse permeability measurements rough surfaces or partial open area of the permeable compression plates can cause similar variations in small scale. This, in turn, can lead to the phenomenon called basis-weight effect, where the measured permeability increases with decreasing thickness (constant porosity) of the sample [Vomhoff et al., 2000, Lindsay and Brady, 1993b]. Related to the in-plane permeability measurements, contradictory observations of the basis-weight effect have been reported in the literature [Lindsay and Brady, 1993b, Vomhoff et al., 2000, Vomhoff, 2000]. For the in-plane permeability measurements the problems may arise due to narrow flow areas and boundary effects, such as flow along the sample

surfaces.

For both the transverse and in-plane permeability, additional experimental error can be caused e.g. by accumulated compression of contractible porous sample in flow direction, leakages bypassing the sample and by gas trapped in the sample or in permeable plates. Inhomogeneity of the sample such as large pores or perforating pin holes can lead to misinterpretation of the data. Altogether, these sources of uncertainty can lead to significant error in the measured value of permeability coefficient for materials such as thin fabrics and paper grades. For this work, the construction of the permeability measurement apparatus, the experimental procedure and the data processing were all designed and manufactured in the purpose of minimising the known sources of uncertainty. Specifically, the experimental procedures for measuring the permeability coefficients in the transverse direction and in the in-plane directions are introduced.

3.1 Devices

The permeability measurement device (PMD) presented in this thesis can be used for measuring Darcian permeability coefficient of soft porous materials under mechanical compression. Permeability measurements can be conducted by liquid or gas flows in the transverse and in the in-plane directions.

A schematic diagram of the PMD is shown in Fig. 3.1. The device includes a sturdy frame, a piston with a upper flow chamber, a moving sample basin with a lower flow chamber and a hydraulic cylinder attached to the sample basin. In addition, the equipment includes pressurised fluid tank, flow control system, flow rate sensors, data acquisition system and a hydraulic pump (not shown in Fig. 3.1). All the components in contact with fluids are made of stainless steel.

The flow sensor used for air measurements is Bronkhorst HI-TEC B.V with maximum flow rate of 10 l/min and reading precision of $\pm$ 0.01 l/min. The pressure difference between the lower and upper chambers (i.e. the total pressure loss over the sample, the sintered plates and the perforated support blocks) is measured using Rosemount 3051S differential pressure sensor with measuring range of 0 - 60 kPa and reading precision of $\pm$ 0.0001 kPa. To take into account the compressibility of air, pressure is also measured at the downstream side of the sample using Keller 41X pressure transducer the maximum reading of 20 kPa and precision 0.1 %. During the measurements, the compressive stress onto the sample is adjusted by a hydraulic hand pump and measured by Keller LEO3 -pressure gauge with measurement precision of $\pm$ 1 kPa. The thickness of the sample is measured by three Sangamo DG1 -displacement sensors arranged 120 degrees apart. The reading precision of each sensor is $\pm$ 4 μm.

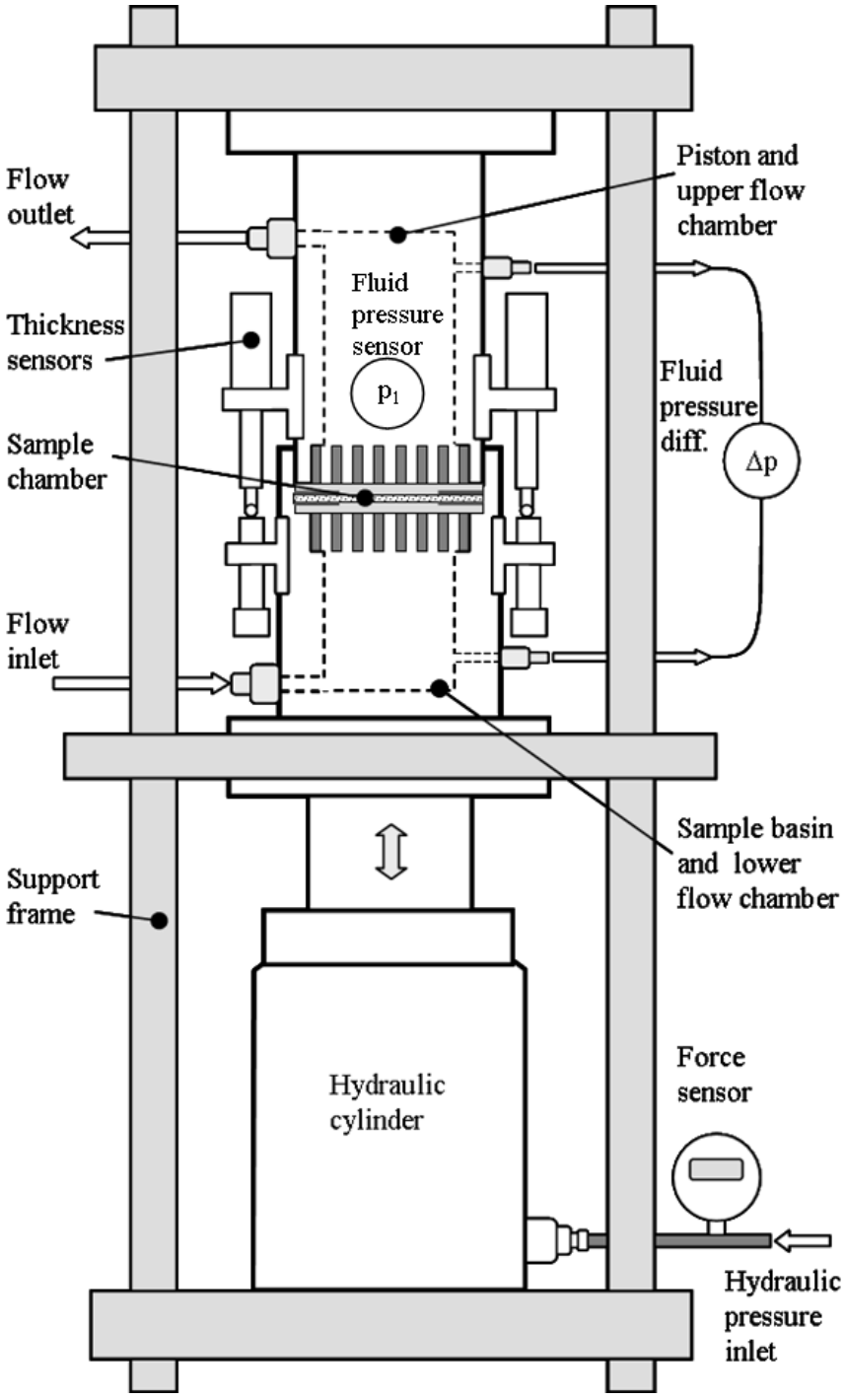

FIGURE 3.1 Schematic illustration of the PMD device for measuring permeability of soft porous materials under compression [Appendix I].

3.2 Transverse permeability

Sample chamber

The sample chamber of PMD for transverse permeability measurements is shown in Fig. 3.2. It includes porous sintered stainless steel plates (see Sec. 3.2) of diameter 90 mm attached to the piston and sample basin, which are both supported by sturdy perforated blocks. The structure is rigid but allows flow from the lower flow chamber through the support and flow distribution blocks, sintered plates and the sample into the upper pressing chamber, and finally to flow transducer. During the transverse measurements the sample is placed between polished sintered plates that conduct support and mechanical compression to the sheet-like sample during the measurements.

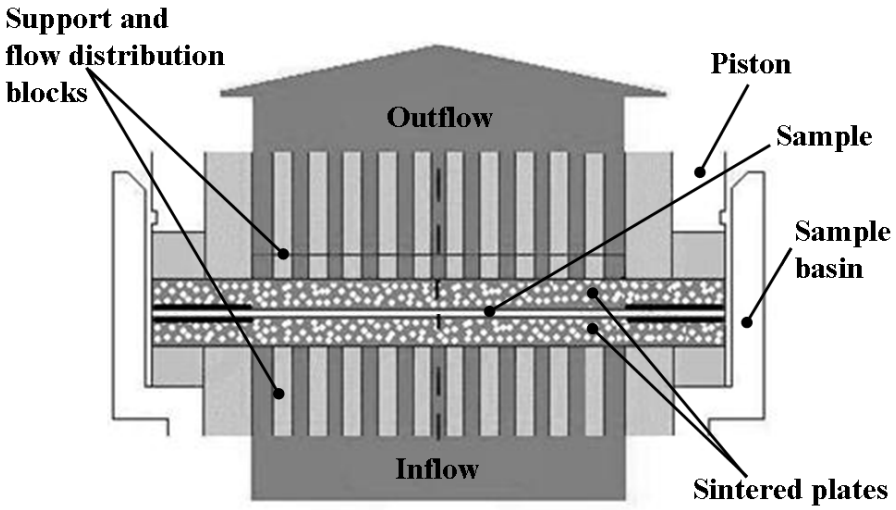

FIGURE 3.2 Illustration of the sample chamber for transverse permeability measurements with sample compressed between the sintered plates [Appendix II].

Compression surfaces

During the measurements the sample must be supported from both upstream and downstream sides to avoid unintentional transformation of the sample structure. On the other hand, the compression pressure must be distributed evenly on the sample. Compression surfaces have apparently a very important role in permeability measurements especially when measuring thin sheet-like samples. The amount of systematic error for thickness measurement depends on the roughness and unevenness of the surfaces. The compression surfaces must be smooth and fine structured but porous enough to produce only small pressure loss and to deliver uniform fluid distribution onto the whole sample area.

Sintered stainless steel plates are composed of small grains solidified by heat and mechanical compression. The compression surfaces were made by first mounting the commercial sintered plates of diameter 90 mm and thickness 4 mm firmly in the sturdy perforated supporting plates. The pores of the sintered plates were electrolytically filled with metallic copper in a copper sulphate solution. Copper plating was done in order to avoid blocking the pores during grinding. The sintered plates together with the supporting plates were attached in a rigid jig with the same shape as the final mounting assembly in the pressing chambers. The surfaces were then carefully ground even and planar.

After grinding the copper was removed from the central region of the plates by electrolysis using inversed polarity. The remaining surface pores in the peripheral region were filled with shrink-resistant metal glue, thus leaving a permeable area of diameter 60 mm in the middle of each plate, see Fig. 3.3. According to test compressions done for pressure-sensitive film, the metallic glue did not change the thickness nor the compressibility of the peripheral region of the plates. Reverse electrolysis corroded slightly the stainless steel parts and made the contact surface more polished. However, the refining grooves on the surface of the sintered plates are still visible in microscopic images, see Fig. 3.3.

According to microscopic observations, the maximum length of the largest surface pores is approximately 0.3 mm which is much less than the mean length of the wood fibers in paper -like samples. The order of sinter grain size is nearly 0.1 mm which is comparable with the thickness of the paper samples. Based on microscopic observations, the surface of the plates is highly planar and the pores are deep and narrow, mode width of the pores being 26 μm. Intrusion of the fibres into the surface pores under mechanical compression is assumed to take place in the small segments of individual fibres rather than macroscopic areas of the sample sheets. Large scale unevenness of the uncompressed plates were tested by profilometry and the variation was found to be $\pm$ 5 μ m. Obliqueness of the plates were corrected by adjusting the measurement device until the plates were parallel to each other.

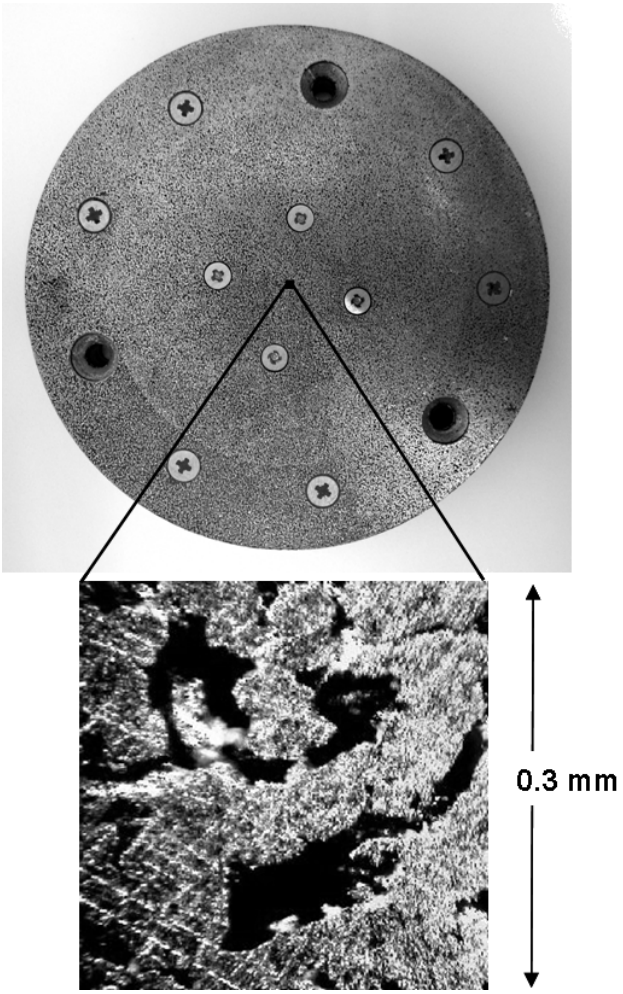

FIGURE 3.3 One of the two identical sintered stainless steel plates with finished surface. The diameter of the plate and the permeable central region are 90 mm and 60 mm, respectively. Inserted microscopic image shows regions of ground steel (with machining grooves), low pores (light area without grooves) and deep pores (dark regions). The relative areas of each region is 40 %, 35 % and 25 %, respectively [Appendix I].

Measurement procedure

In the beginning of each measurement, a circular sample of diameter of 90 mm was placed in the permeability chamber and the sintered plates were brought into contact with the sample. The contact point was indicated by a slight increase of compressing force. The pressure difference over the sample was first measured as a function of air flow rate to verify that the flow condition indeed is in the linear regime where Darcy's law is valid. Based on the results of this preliminary measurement, the air pressure difference was adjusted such that the flow rate is well in this linear region for the nearly uncompressed sample, giving upstream pressure typically around 20 kPa. The compressing force was then gradually increased typically in steps of 1 kN until the maximum of 40 kN (corresponding to mechanical pressure step of approximately 0.16 MPa) keeping the air pressure difference approximately constant. Notice that since the flow rate decreases with increasing compression, the flow condition remains in the linear regime throughout the compression experiment. After each increase of compressing force, a short relaxation time was allowed for the sample, and the steady state values of flow rate, pressure difference, sample thickness and compressing force were recorded. The ratio between air pressure difference and compressive stress was kept small (in all cases less than 0.15) in order to avoid non-uniform compaction of the sample due to network forces. After certain data corrections the value of the transverse permeability coefficient k_{zz} at each state of compression was calculated using Darcy's law for compressible fluid flow, Eq. (2.8). The effect of the compressibility was typically found to be 0–5 % for the transverse measurements.

Data correction and uncertainty estimation

The particular objective of the development of the PMD was to obtain a method that would be applicable especially for sheet-like samples. Special effort was made in eliminating the known sources of inaccuracy both within the measuring device and within the experimental procedure, and for correcting the data for secondary flow effects. The measured values of thickness, pressure loss and flow rate must be corrected for effects caused by elastic deformation of the device, for pressure loss due to device geometry and for the effective flow area through the sample, respectively.

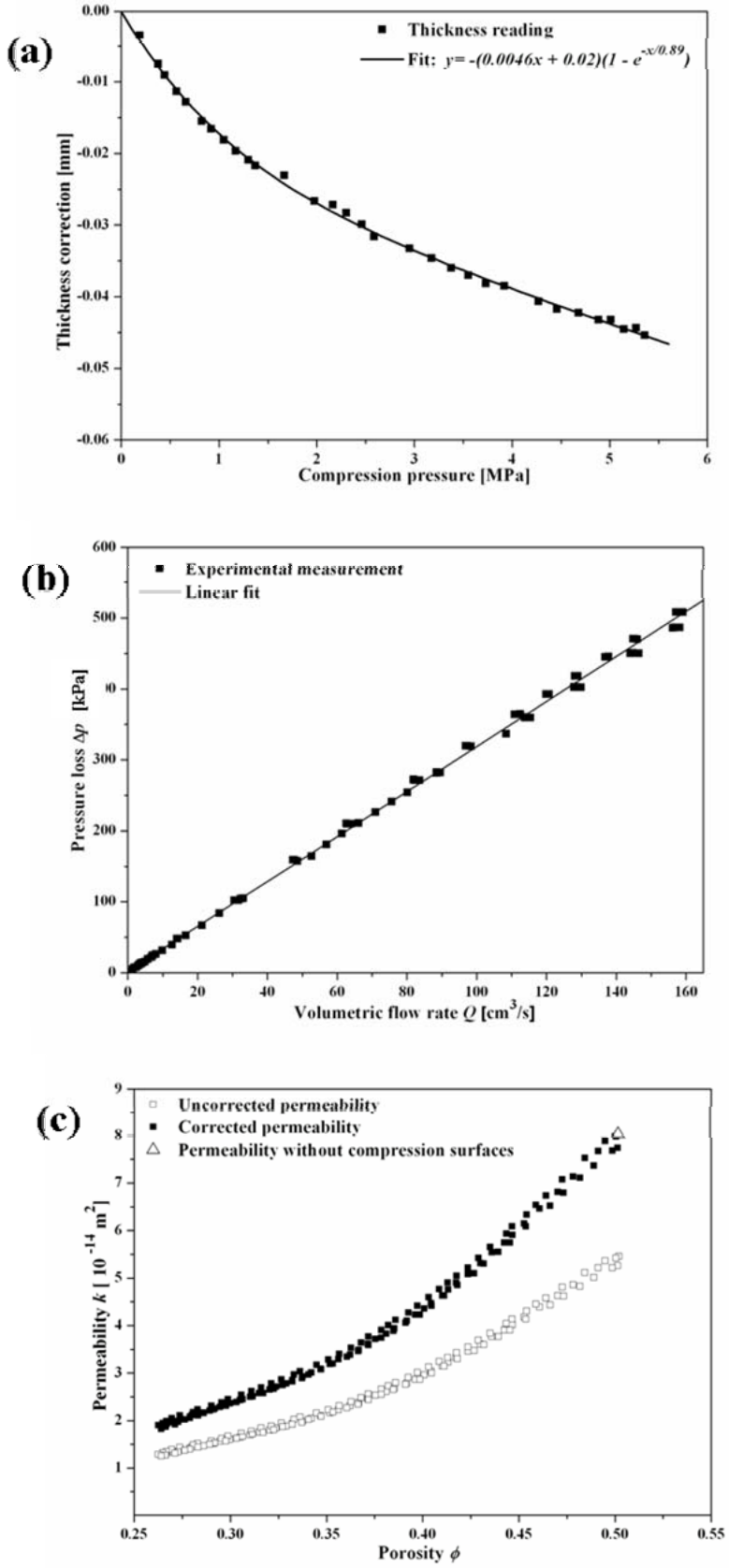

FIGURE 3.4 Examples of correction data sets. (a) Thickness correction vs. compression pressure with a fitting function. (b) Measured data for device loss, i.e. pressure loss vs. volumetric flow rate for an empty device. (c) Example of a flow area correction showing the uncorrected permeability data (calculated using the area A_0 of the entire permeable central region of the sintered plates), the value of permeability for uncompressed sample and the data corrected for the effective flow area A_{eff} [Appendix I].

The correction to thickness measurement was determined by first bringing the sintered plates in contact (using a very small loading force) and adjusting the reading of each displacement transducer to zero. The mechanical load was then gradually increased to a maximum value of 40 kN while recording the readings of the displacement transducers. The average reading of the three transducers is shown in Fig. 3.4a together with a fitting function that is a combination of first order polynomial and exponential functions. This compression pressure dependent correction is subtracted from the measured thickness of the actual experiments. The thickness correction was verified occasionally during measurements and redetermined after disassembly and reassembly of any mechanical part of the frame of the device (see Fig. 3.1). The typical effect of the thickness correction at the maximum mechanical compression load is 10 % - 40 % of the measured thickness of the sample.

The air pressure difference is measured between the lower and upper flow chambers. In addition to the loss caused by the sample, the measured pressure difference is thereby affected also by the loss appearing in supporting structures and sintered plates. The influence of the structure was therefore determined by measuring the loss coefficient i.e. the ratio between pressure difference and volumetric flow rate for the empty device and subtracting the effect from the measurement results. Fig. 3.4b shows the measured pressure difference as a function of flow rate for empty device and clearly indicates linear behaviour that is in accordance with Darcy's law. The typical effect of this correction is 10 % - 40 % of the measured pressure difference.

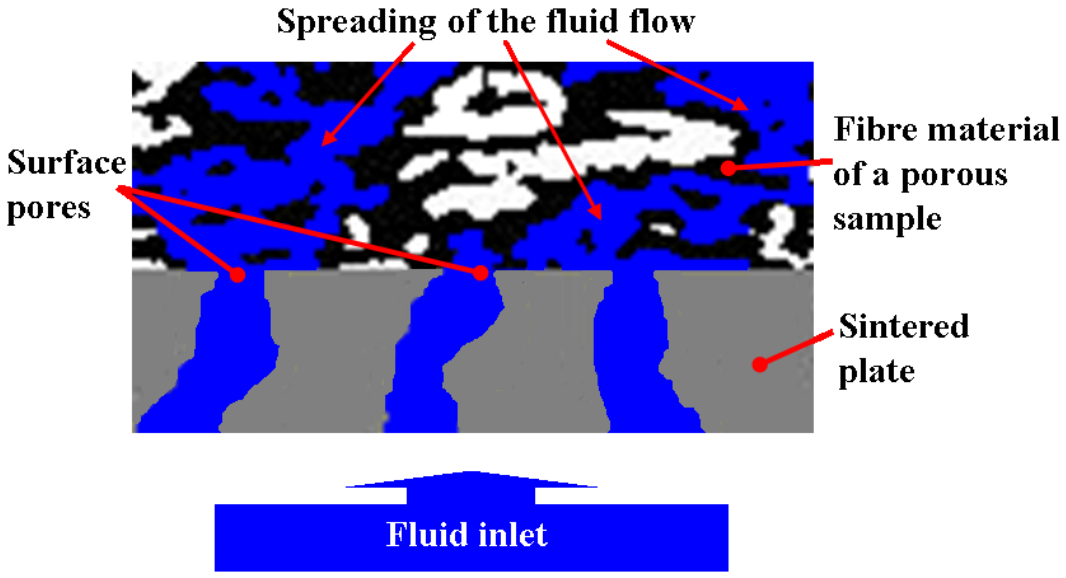

FIGURE 3.5 Spreading of fluid flow in a porous sample.

The surface of the sintered plates is not completely open for flow, i.e. the flow area measured from the surface pores of the sintered plate is smaller than the perme-

able central region A_0 of diameter 60 mm. On the other hand, the fluid emanating from the pores of the sintered plates can spread in the sample in a manner that depends on the pore structure of also the sample, see Fig. 3.5. The actual area of flow through the sample is therefore not exactly known. The effective flow area, A_{eff} can be found for each type of material by measuring the permeability of an uncompressed sample with no sintered plates assembled in the device. In this experiment, the sample is compressed only at its peripheral part to prevent any flow on that region, and the central part is fully open for flow. The effective flow area is then determined such that the value of permeability found in actual compression experiments (extrapolated to zero compression) coincides with that measured without sintered plates. Notice, that a small degree of compression is necessary for a meaningful measurement with sintered plates in order to avoid leakages along the surfaces. An example of the resulting correction to original data is shown in Fig. 3.4c. Clearly, this correction procedure is based on an assumption that the effective flow area does not vary significantly with the degree of compression. Typical values for the area ratio A_{eff}/A_0 are between 0.6 and 0.9 for fibrous porous samples.

The most important sources of error involved in the present method appear to be the error of the thickness measurement and the uncertainties included in various corrections applied in the measured results. Rather conservative assumption is that the relative uncertainties of the corrections made to thickness, flow area and pressure difference are 40 %, 40 % and 10 %, respectively. The maximum relative error of the permeability results can be estimated using equation [Taylor, 1997]

$$\frac{\delta k_{ii}}{k_{ii}} = \frac{\delta C_{L_{ii}}}{L_{ii}} + \frac{\delta C_A}{A} + \frac{\delta C_P}{P}, \tag{3.1}$$

where $\delta C_{L_{ii}}$, δC_A and δC_P are the error values for thickness, flow area and pressure measurements after applied data corrections.

The upper limit of the error is met with thin samples under high mechanical load. The effect of the thickness correction for thin samples is typically 40 %. The thickness values of thin samples are often order of 100 μm. Under high compression pressures the thickness correction is approximately 40 μm with error of $\delta C_{L_{ii}} = \pm$ 16 μm. The amount of flow area correction for sheet-like samples is about 30 %. The area of the sintered plates is 0.00284 m^2 and thus the error of the flow area is $\delta C_A = \pm$ 0.00034 m^2. The effect of pressure loss correction for compressed samples is estimated to be 20 %. The pressure loss during the experiments is typically of the order of 20 kPa and the amout of the maximum instrument-specific correction is 5 kPa with error of $\delta C_P = \pm$ 0.5 kPa. Utilising Eq. (3.1) and the preceding error assumptions the estimation of the maximum uncertainty of the present results is less than 35 %. With thicker samples and with thin samples under low or moderate loading, the relative uncertainty is less than the above-mentioned maximum value. Taking into account the large variation of permeability between different materials

and even with the same material under different states of deformation, this accuracy can be considered satisfactory.

3.3 In-plane permeability

Sample chamber

The only difference between the transverse and in-plane measurement set-up is the sample chamber. A schematic illustration of the modified sample chamber for in-plane flows is presented in Fig. 3.6a. A rectangular sample of dimensions 70 mm x (5 - 15) mm, is attached between smooth stainless steel plates presented in Fig. 3.6b. The gaps between the sample and the compression plates are sealed using double sided tapes and elastic sealing compound. This is done in order to avoid flow around the sample and to minimise contact boundary effects. The long side of the rectangular sample sheet is perpendicular to the main flow direction.

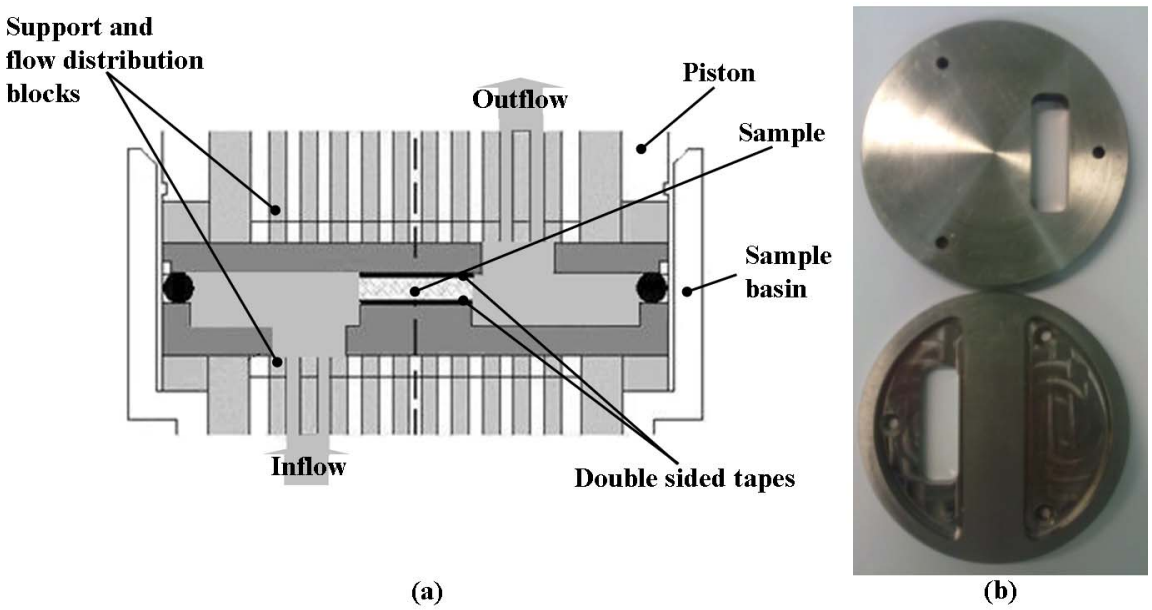

FIGURE 3.6 (a) A detailed illustration of the sample chamber for in-plane permeability measurements with sample placed between double sided tapes to avoid leakages along the sample surfaces. (b) Upper and lower compression plates [Appendix II].

Measurement procedure

The measurement procedure was conducted similarly as during the transverse flow measurements. The only significant difference was the sample preparation. In order to increase the flow area, the sample sheets (with thickness in the range 100–500

μm) were sandwiched as stacks of 3–10 layers by plastic impermeable double-sided tapes. The sample stacks were then cut to the suitable dimensions. According to the microscopy (see Fig. 3.7) and micro-tomography observations the pores on the cut vertical edges were open for the fluid flow and significant gaps between the tapes and samples did not exist.

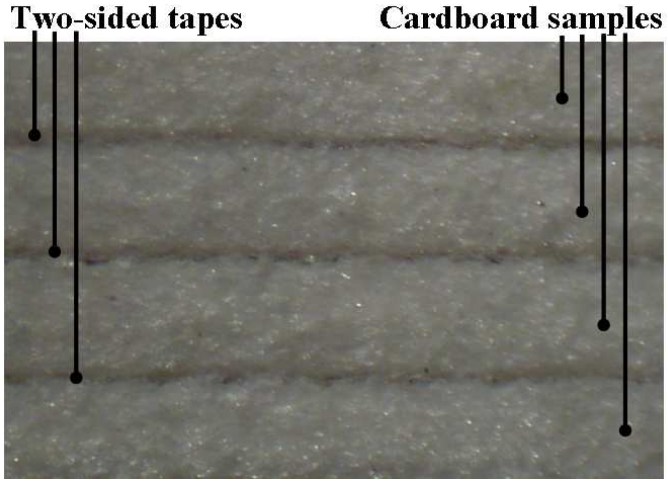

FIGURE 3.7 A microscopy image of a stack of cardboard samples [Alaraudanjoki, 2008].

In the beginning of each measurement, a rectangular sample sheet or a sample stack was placed in the permeability chamber, see Fig. 3.6. The sample was carefully taped between the rectangular supporting plates by double sided tapes and the contact was confirmed by a slight increase of compressing force. The pressure difference over the sample was first measured as a function of air flow rate to verify that the flow condition is in the linear flow regime. For the actual permeability measurements, the average upstream pressure was typically selected to be around 30 kPa – 50 kPa. After each increase of compressing force, a short relaxation time was allowed for the sample. The steady state values of flow rate, pressure difference, sample thickness and compressing force were recorded. Finally, the value of the in-plane permeability coefficient k_{xx} (or k_{yy}) at each state of compression was calculated using Darcy's law for compressible fluid flow, Eq. (2.8). The effect of the compressibility was typically found to be 5–15 % for the in-plane measurements.

Data correction and uncertainty estimation

For the in-plane measurements the pressure loss caused by the device is negligible due to the geometry of the sample chamber, see Fig. 3.6. The whole inlet edge of a sample is open for fluid flow and the concept of the effective flow area is not needed. However, the flow area is calculated utilising the thickness measurement data. The

thickness correction was estimated similarly as in the case of the transverse measurement set-up, but taking the compressibility of the two-sided tapes into account. The thickness correction was determined by first bringing the supporting plates in contact with the two sided tapes (using a very small loading force) and adjusting the reading of each displacement transducer to zero. The mechanical load was then gradually increased while recording the readings of the displacement transducers. This compression pressure dependent correction is again subtracted from the measured thickness of the actual experiments.

In the case of in-plane flow measurements, the terms for uncertainties of flow area and pressure loss in Eq. (3.1) are neglected. The uncertainty of the thickness measurement data (which determines the flow area) is estimated as in the case of transversal measurements. The maximum uncertainty of the present results is estimated to be less than 20 %. This upper limit is met with thin samples under high mechanical load. With thicker samples and with thin samples under low or moderate loading, the relative uncertainty is less than this maximum value.

Chapter 4

Numerical permeability analysis based on tomographic reconstructions

Flow through the pore space of complex structures have been widely studied also with computational methods, e.g. Refs [Koponen et al., 1996, Succi, 2001, Aaltosalmi et al., 2004, Arns et al., 2004, Belov et al., 2004, Kerwald, 2004, Ramaswamy et al., 2004, Nordlund et al., 2005, Verleye et al., 2005, Levitz, 2005, Hyväluoma et al., 2006, Lundström et al., 2005, Versaevel et al., 2006, White et al., 2006, Keehm et al., 2006, Fourie et al., 2007, Nordlund et al., 2007, Wiegmann, 2007, Jaganathan et al., 2007, Verleye et al., 2007, Vidal et al., 2008, Andersson et al., 2009, Frishfelds et al., 2009]. Some of these recently published studies utilise computerised x-ray micro-tomography (CXμT) reconstructions in combination with numerical methods. In this part of the work, creeping flow through porous materials is solved by utilising the lattice Boltzmann method (LBM) with a numerical grid given by x-ray tomographic reconstructions of actual material samples. The LBM is based on solving the discrete Boltzmann equation instead of the standard continuum flow equations.

In this chapter, special attention is paid for developing the procedures for tomographic imaging, image processing and numerical analysis in particular applications related to fibrous porous heterogeneous materials. The reliability of the numerical analysis results are estimated by comparing them with the experimental results or in some cases with the corresponding analytical values. The numerical LBM results are also compared with the results obtained by other numerical methods, namely finite-element method (FEM) and finite-difference method (FDM).

4.1 X-ray micro-tomographic imaging

Authentic simulation geometries were obtained by utilising computerised CXμT. Both synchrotron based x-ray beams and conventional x-ray tubes are used as the radiation source. The adequate resolution and the overall quality of the images depend on the techniques used. In this work, a table-top scanner (Sky-Scan 1172) based

on x-ray tube, and a tomographic imaging facility ID19 of the European Synchrotron Radiation Facility (ESRF) were used, see Fig. 4.1.

The voxel resolution of the table-top device can be varied from a few micrometres up to few tens of micrometres. Here the voxel resolution of the tomographic reconstructions produced by the table top scanner was 4.48 μm and the diameter of the samples 6 mm. The table top scanner was utilised for imaging the structures of the synthetic non-woven felt and the wet pressing felt. With the set-up used at ID19 facility, the voxel resolution was fixed to 0.7 μm and the diameter of the full tomographic reconstruction was 1.4 mm. The ID19 facility was utilised for scanning the cardboard and the paper -like samples. Specific plastic sample holders were designed and manufactured to enable scannings of the samples under adjustable static compression levels, see Figs 4.1b and c.

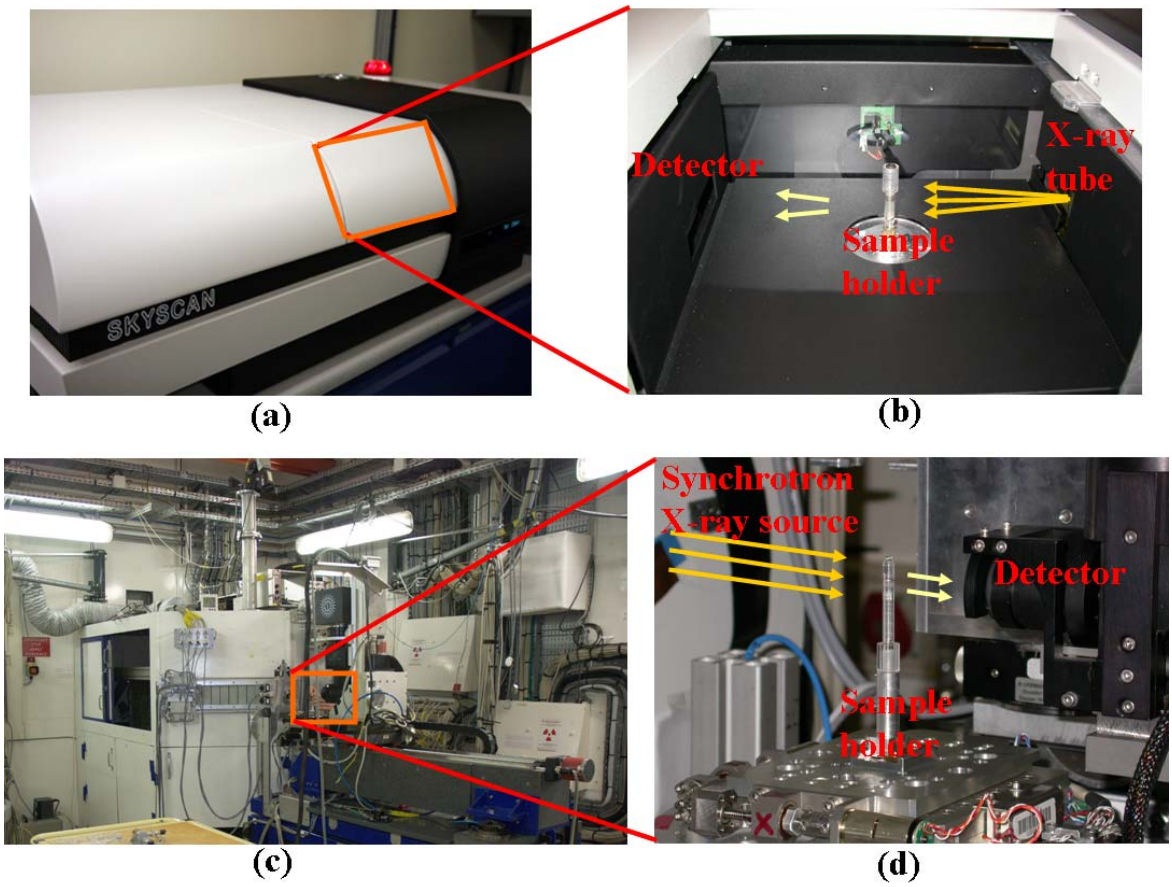

FIGURE 4.1 The tomographic devices used in this work. (a) SkyScan1172 tomographic scanner and (b) insert to sample chamber. (c) Hutch of the beam line ID-19 and (d) insert to show sample holder. Direction of the X-ray beam is presented for both the scanning set-ups.

4.2 Implementation of the lattice Boltzmann method

The LBM is particularly well suited for solving fluid flow in complex geometries such as in the pore space of irregular porous media [Succi et al., 1989, Koponen et al., 1996, Manwart et al., 2002, Martys and Hagedorn, 2002, Arns et al., 2004, Belov et al., 2004, Kerwald, 2004, Kutay et al., 2006, White et al., 2006, Eker and Akin, 2006, Pan et al., 2006, Vidal et al., 2008]. This advantage of the method follows mainly from straightforward implementation of the no-slip boundary condition on fluid-solid interface. In the LBM scheme used in this work, the no-slip condition was realised by utilising the standard halfway bounce-back boundary condition. Furthermore, the particular D3Q19 model of LBM with the linear two relaxation time approximation of the Boltzmann equation introduced by Ginzburg et al. [Ginzburg and d'Humiéres, 2003, Ginzburg et al., 2008] was used. It appears that this approach avoids the problem of dependence of permeability on viscosity that is encountered within more simple models such as the single relaxation time Bhatnagar-Gross-Krook (BGK) model [Bhatnagar et al., 1954, Ginzburg and d'Humiéres, 2003, Hayashi, 2003, Pan et al., 2006, Ginzburg, 2008].

Numerical grid from tomographic reconstructions

Suitable subvolumes were cropped out of the full CXμT reconstructions, filtered by variance-weighted mean filter [Gonzalez and Woods, 2002] and thresholded to yield a binary image including the solid material and the pore space. A typical subvolume size thus obtained for the felt samples were 500x500x(300-420) voxels, where the last dimension is for the thickness of the sample and varies with the degree of compression. For paper -like samples, the grid sizes were 300x300x(100-200) voxels. For cardboard -like samples, the typical grid sizes varied from 300x300x(100-200) voxels to 1000x1000x(300-600) voxels. A visualisation of a binarised tomographic subvolume is presented in Fig. 4.2a. The processed tomographic subvolumes were used as a uniform cubic grid (voxels of the tomographic image) for numerical solution of flow through the pore spaces. Figure 4.2b-c demonstrate the cubic numerical grid based on a tomographic reconstruction. Within the numerical analysis by LBM the velocities and pressures are defined at these lattice points (the centre points of the cubic unit cells).

The binarisation processes of the CXμT reconstructions is known to affect the numerical analyses results to some extent [Stock, 2009]. However, the major source of uncertainty in numerical permeability analysis is the statistical error caused by the heterogeneous structure of the materials together with the small size of the samples limited by the computational resources available. In order to minimize the effect of local variations in heterogeneous materials, representative samples for the micro-tomography were selected carefully from larger samples sheets. For example, an optical formation map of the paper and cardboard sheets were obtained using

digital imaging with transillumination. The tomographic samples were then taken from locations of the sheet where the local optical density equals the mean optical density of the sheet. Also, the limited resolution of the tomographic reconstructions have a contribution to the uncertainty on the numerical results. This discretisation error is discussed later in Sec. 4.3.

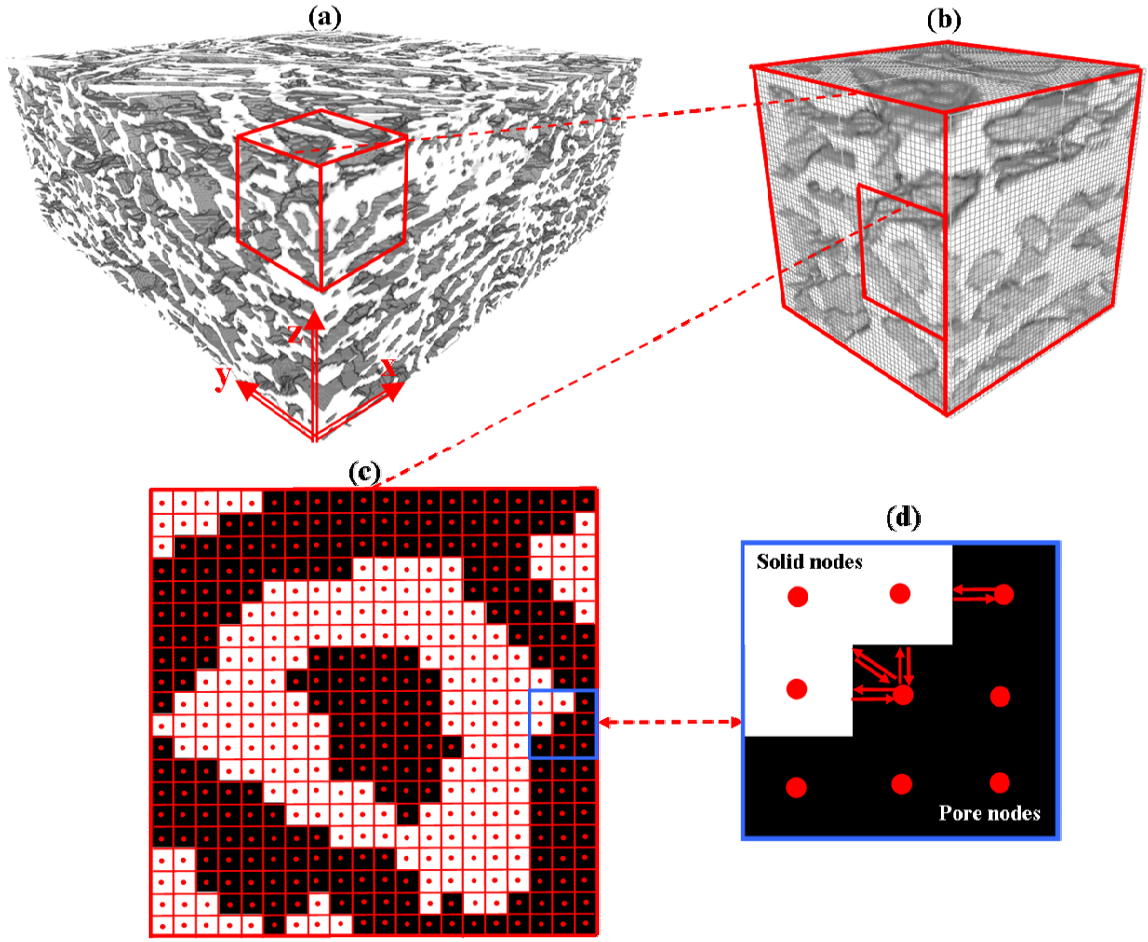

FIGURE 4.2 Schematic illustrations of computational grid based on a tomographic reconstruction of hardwood paper sample: typical binarised subvolume of a CXμT reconstruction for numerical analysis (a) (voxel resolution of the reconstruction is 0.7 μm), insert to visualise the cubic grid of a small segment of the subvolume (b), insert to show the lattice points in the real micro-scale structure (c) and implementation of the standard halfway bounce-back boundary condition (d).

Body force and boundary conditions

During the numerical permeability analysis the body force mimics the upstream pressure of the experimental measurements. The computed values of permeability are, in principle, independent on the selected values of body force as long as the resulting flow is well in the creeping flow regime.

The standard halfway bounce-back boundary condition was utilised to implement the no-slip boundary condition on the fluid-solid interface, (see 4.2d).

On the sides parallel to the main flow direction, periodic or reflection symmetry boundary condition was applied. Periodic condition was used for flow analysis through computationally generated sample models and reflection symmetry for the tomographic reconstructions. However, in the cases where LBM results were compared with the results obtained by FDM, the periodic condition was enforced also for the tomographic geometries.

Periodic boundary condition was applied in the flow direction. In order to attenuate undesired propagation of the downstream information to the upstream flow, thin layers of fluid were added on the upstream and downstream boundaries of the sample and momentum averaging was applied on a single cross-section of the fluid layer. These additional fluid layers also mimic the experimental measurement conditions, where the boundaries of the samples in the flow direction are in principle open for flow. In Fig. 4.3 are two visualisations of the flow speed (norm of the velocity vector) fields (in z and x directions) through the subvolume that was introduced in the Fig. 2.1.

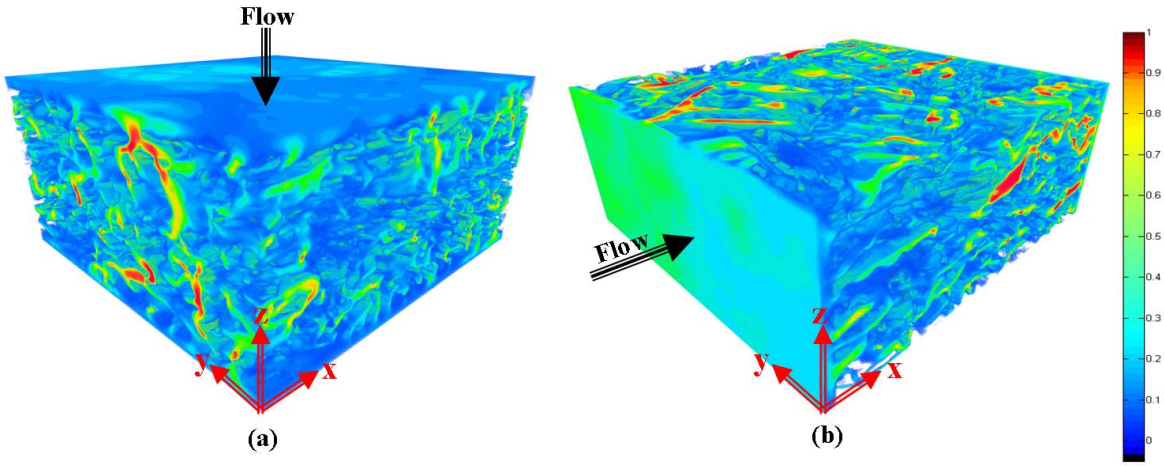

FIGURE 4.3 Visualisation of numerically solved flow speed (norm of the velocity vector) fields through the hardwood paper subvolume introduced in Figs 2.1 and 4.8: fluid flow in z-direction (a) and in x-direction (b). Also shown are the additional ten fluid layers on both sides of the subvolumes in flow direction. Red and blue colours indicate high and low flow speed, respectively

4.3 Comparison and testing

Regular geometries: comparison to analytical, FEM and FDM results

Numerical LBM permeability results for computationally generated regular rod geometries were compared with the values obtained by two other numerical methods, namely FEM and FDM. The computationally generated regular geometries consist of rods with circular and square cross sections. The numerical analyses are conducted for hexagonal arrays or rods in four different porosity levels, namely 60 %, 70 %, 80 % and 90 %. In Fig. 4.4 are examples of visualisations of the flow speed fields solved numerically using LBM in the pore space of hexagonal rod arrays in porosity level of 70 %. Presented are the main flow directions parallel to rods z, and perpendicular to rods y and x. The numerical FEM and FDM analyses for the same geometries were performed by Geindreau et al. [2009].

Comparison between the numerical values of permeability for hexagonal arrays of square rods in different porosity levels is shown in Table 4.1. The maximum deviation between the numerical values given by the LBM, FEM and FDM is less than 2.2 %.

TABLE 4.1 Comparison of numerical values of dimensionless permeability in three coordinate directions for hexagonal array of cylinders with square cross section ($L = 1/2$ side length of the cylinder cross section). Also is given the deviation $(k_{max} - k_{min})/k_{min}$ between various numerical results [Appendix III], [Geindreau et al., 2009].

Por. [%]	Dimensionless permeability											
	k_{xx}/L^2				k_{yy}/L^2				k_{zz}/L^2			
	LBM	FEM	FDM	Dev. [%]	LBM	FEM	FDM	Dev. [%]	LBM	FEM	FDM	Dev. [%]
60	0.0330	0.0330	0.0337	1.9	0.0420	0.0420	0.0426	1.5	0.0955	0.0969	0.0970	2.1
70	0.0994	0.0993	0.101	1.4	0.111	0.111	0.112	1.2	0.245	0.247	0.249	1.8
80	0.321	0.321	0.324	1.0	0.331	0.332	0.335	1.1	0.719	0.723	0.730	1.5
90	1.39	1.39	1.40	0.8	1.40	1.40	1.41	0.7	2.95	2.98	2.99	1.4

For certain geometries the numerical results were compared with the analytical ones. Analytical permeability results for the flow parallel to the rods (k_{zz}) are calculated by the equation introduced by Drummond and Tahir [1984], Eq. (2.15). Semi-analytical tabulated results for the permeability values for the flow perpendicular to the rods (k_{xx} and k_{yy}) are given by Sangani and Acrivos [1982]. The agreement between the numerical and analytical results is good, as indicated by Fig. 4.5.

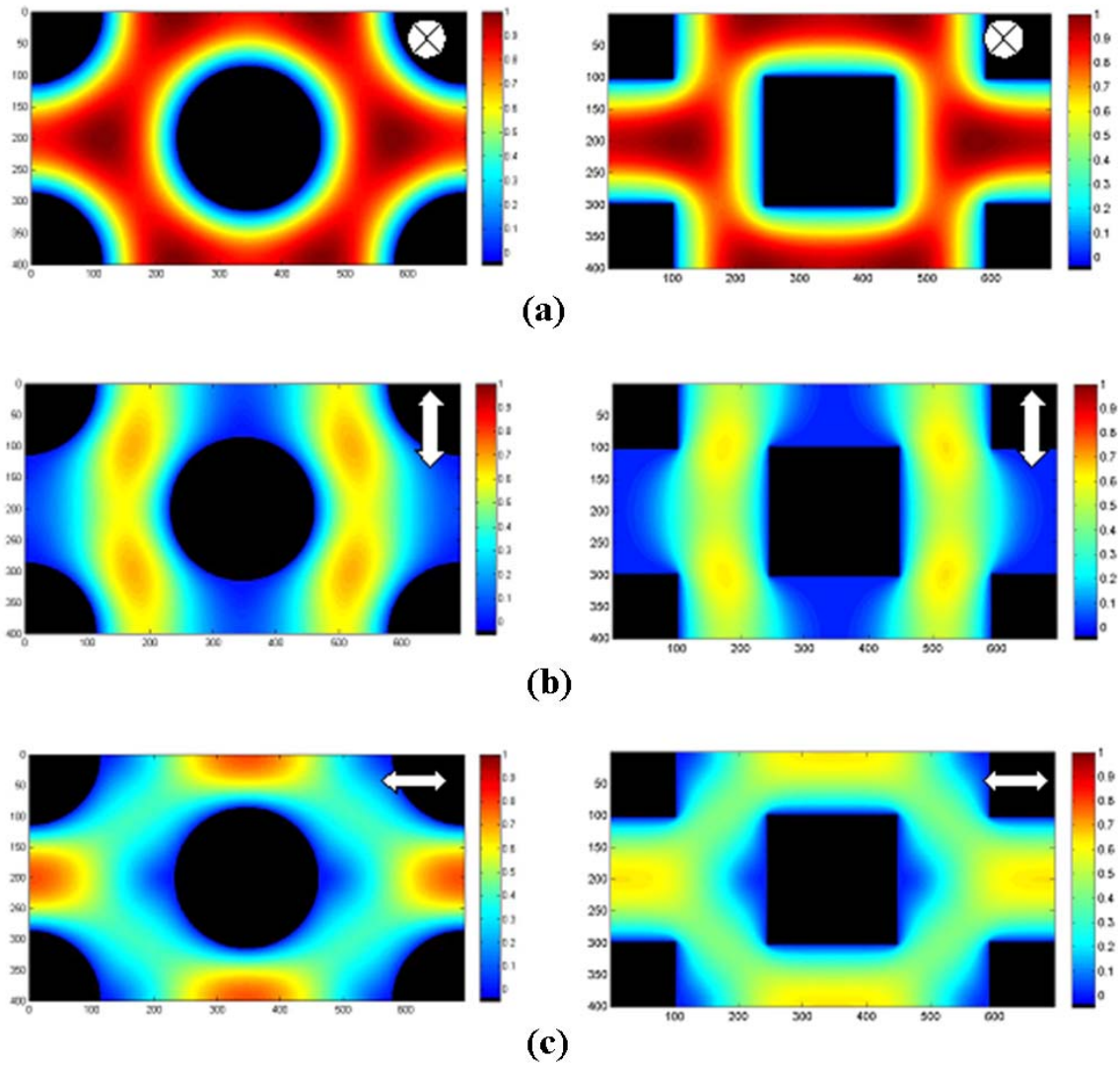

FIGURE 4.4 Visualisations of numerically solved flow speed (norm of the velocity vector) fields through hexagonal arrays of (circular and square cross-section) cylinders at 70 % porosity level. The main flows are in (a) z, (b) y and (c) x -directions. Red and blue colours indicate high and low flow speed, respectively. The same colour represents the same flow speed in all the visualisations.

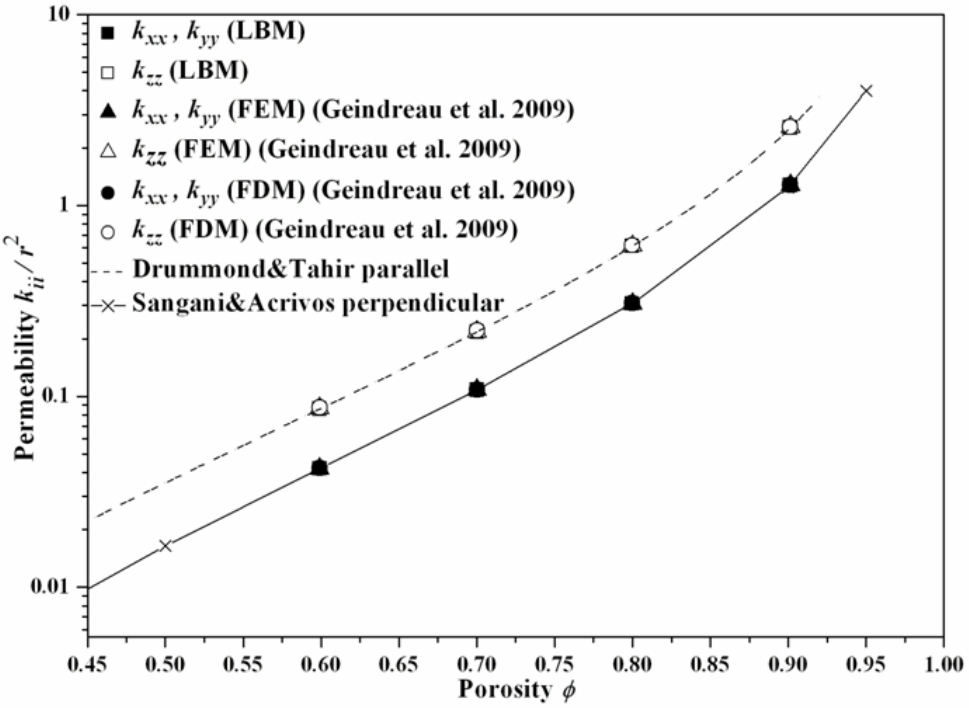

FIGURE 4.5 Numerical and analytical values of dimensionless permeability (for flows perpendicular and parallel to rods) for hexagonal array of circular cylinders (with radius r) at different porosity levels [Appendix III] [Geindreau et al., 2009].

Estimation of discretisation uncertainty

The finite resolution of the tomographic reconstruction, as set by hardware limitations or by trade-off between resolution and sample size, also sets a practical upper limit for the density of the grid for numerical flow analysis. The straightforward method for grid generation in which the numerical grid is a regular cubic lattice based on the tomographic image itself is used. The unit cell of the numerical grid thus equals the cubic voxel of the digital tomographic reconstruction. In order to estimate the accuracy of the solution obtained using such a relatively coarse numerical grid, the values of permeability coefficients for a computationally generated model geometries were analysed. For estimating the discretisation uncertainty, high and low density grids of square array of circular cylinders at porosity levels of 60 %, 70 %, 80 % and 90 % were analysed. Numerical permeability analyses were conducted for main flow parallel and perpendicular to the rods, z and x, respectively. The resolution of the low density grid was selected such that the diameter of the rods in grid units corresponded the typical diameter of the fibres in units of voxel size of the tomographic reconstructions. Visualisation of the flow speed fields through the high and low density grids (at porosity levels of approximately 70 %) are shown in the Fig. 4.6.

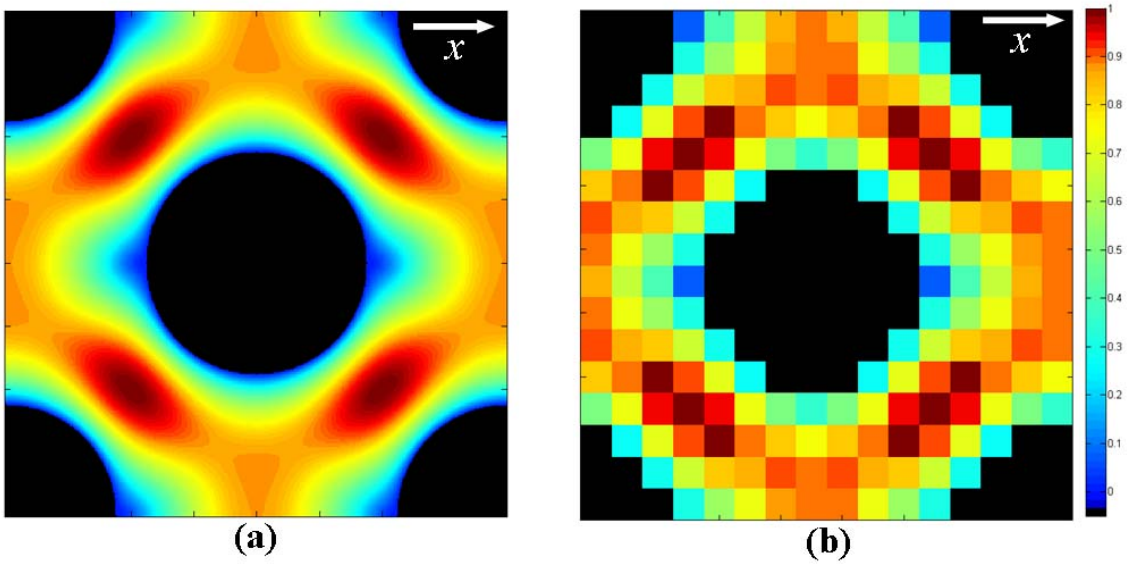

FIGURE 4.6 Flow speed (norm of the velocity vector) solved using high density grid (a) and low density grid (b) for an array of circular cylinders (porosities 70 and 71 %, respectively). The mean flow is in the x direction. Red and blue colours indicate high and low flow speed, respectively [Appendix III].

The computed results for permeability obtained with high and low density grids for square array of circular cylinders at different values of porosity are shown in Fig. 4.7 together with corresponding analytical results. Analytical values for flow

parallel to the cylinders (z direction) are given by Eq. 2.15 [Drummont and Tahir, 1984] and the semi-analytical results for flow perpendicular to the cylinders (in $x-y$ plane) by tabulated results of Sangani and Acrivos [1982]. The numerical results obtained using the high density grid closely agree with the analytical predictions. The numerical results obtained with the low-density grid deviate from the analytical and more accurate numerical results. Including all the cases analysed, the maximum relative deviation between the values of permeability obtained using low density numerical grid as compared to either theoretical or high resolution numerical results was, however, less than 10 %.

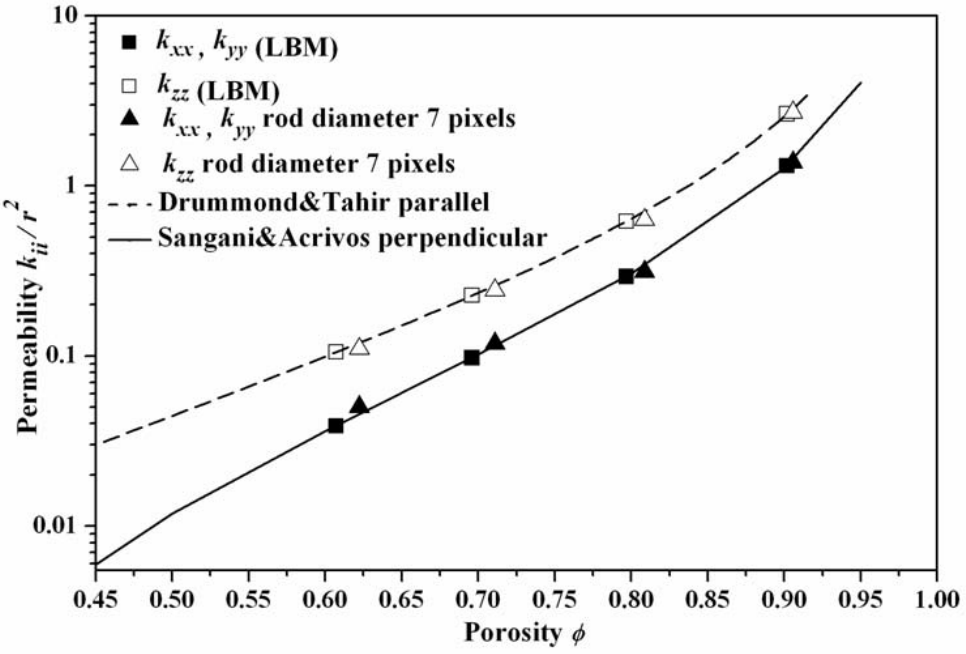

FIGURE 4.7 Numerical and analytical values of dimensionless permeability, for flows perpendicular k_{zz} and parallel $k_{xx} = k_{yy}$ to the rods for square array of circular cylinders at different porosity levels [Appendix III].

LBM in porous heterogeneous materials: comparison to FDM and experimental results

Numerical analyses were conducted for the tomographic subvolumes of a synthetic non-woven felt and a hardwood paper samples. The felt material consists of nearly cylindrical smooth fibres of average diameter 34 μm. The fibres are curved to some extent and have only weak tendency to be oriented in the plane of the felt. Within that plane, the orientation is isotropic, in average. The structure of hardwood paper and the internal shape of individual wood fibres are considerably more complicated

than those of the non-woven felt. The hardwood paper handsheet is manufactured from mechanical hardwood pulp and it has grammage of 56 g/m^2 and thickness of 0.106 mm. Wood fibres typically include a lumen and a cell wall with flattened irregular cross-section. The wall thickness and the average diameter of the fibres were found to be approximately 4 μm and 20 μm, respectively. In paper -like materials, the fibres are strongly oriented towards the plane of paper but are also isotropically oriented within that plane [Rolland du Roscoat et al., 2007].

Visualisation of a subvolume of the synthetic non-woven felt and the 3D flow speed field through it for main flow in z direction is presented in Fig. 4.8. Permeability values were analysed in the directions x, y and z (see the coordinate convention in 4.8a). Visualisations of the hardwood paper subvolume and the 3D flow speed fields are presented in the Figs 2.1 and 4.3, respectively. Detailed 2D visualisations of the flow speed fields inside the samples are shown in Fig. 4.9.

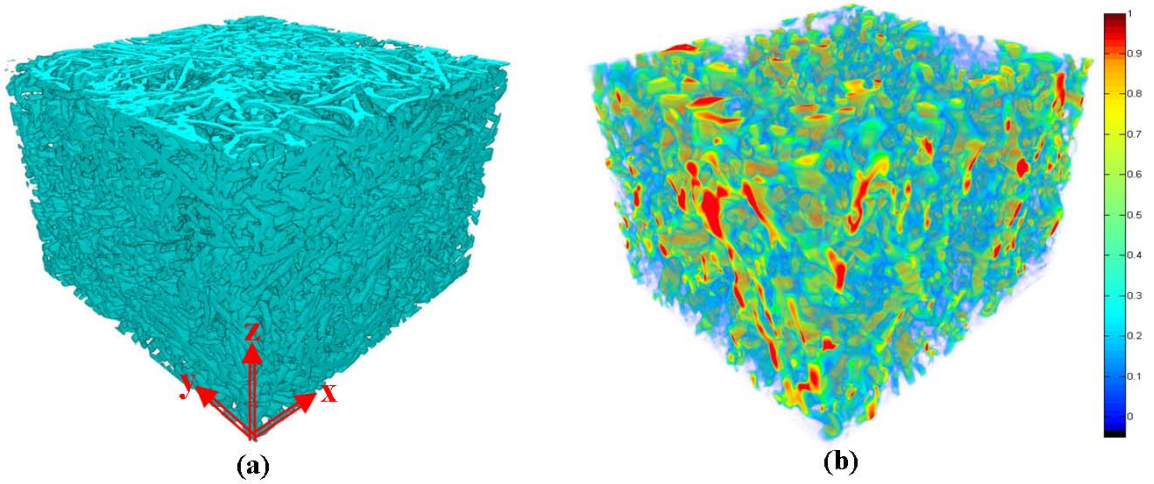

FIGURE 4.8 Visualisations of a tomographic subvolume of synthetic non-woven felt material (a) and the flow speed (norm of the velocity vector) field simulated in the z -direction through it (b). Additional fluid layers are removed from the visualisation. In (b), red and blue colours indicate high and low flow speed, respectively.

The numerical permeability results were compared with the experimental data for the same materials. Numerical and experimental results of permeability in three directions for synthetic non-woven felt and hardwood paper samples are summarised in Table 4.2. In this case the numerical results obtained by the two methods, LBM and FDM, deviate from each other more than in the case of regular arrays. Most likely, this is just an indication of both methods being less accurate in the complex geometries. Notice that the boundary of the flow domain (pore space) is in this case known only to the accuracy of the tomographic reconstruction. It is thus obvious that the relatively coarse cubic grid provided directly by the tomographic images does not allow for very accurate solution of flow especially near the solid boundaries and in narrow passages.

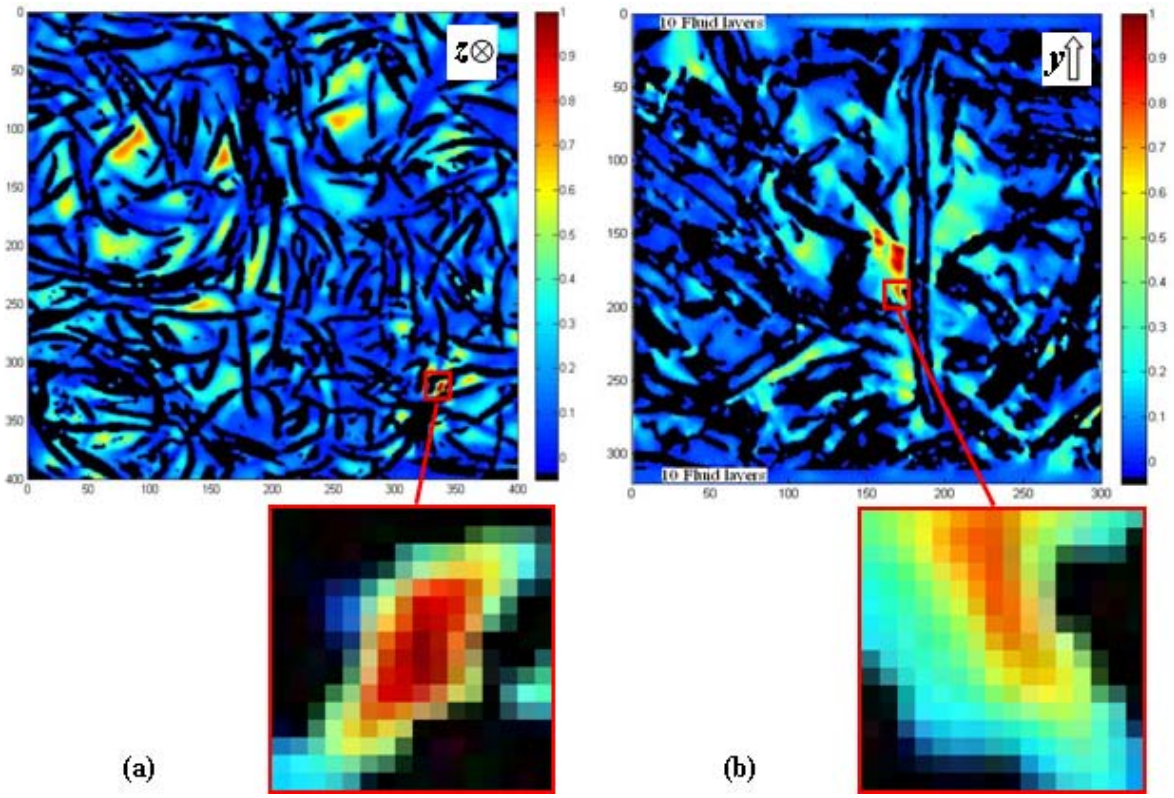

FIGURE 4.9 Numerically solved flow field in synthetic non-woven felt (a) and hardwood paper (b). Shown is the scaled flow speed (norm of the velocity vector) on single 2D cross sections ($x - y$ plane) of the full 3D solution space within the actual tomographic subsamples. Red and blue colours indicate high and low flow speed, respectively. Solid material is coloured black. In (a) mean velocity is in the z direction. In (b) mean flow is in the y direction. Notice also the fluid layers visible at the upstream and downstream sides of the hardwood paper sample. Inserts show details of the pore structure and flow velocity pattern with resolution of the numerical grid given by the tomographic reconstructions (4.84 μm and 0.7 μm for (a) and (b), respectively) [Appendix III].

The most important single source of uncertainty in the present numerical results most likely is the rather poor statistics obtained due to the low number and small size of subsamples. Even though several subsamples were analysed, the variation of permeability value thus obtained (and indicated in Table 4.2) does not necessarily correspond to the total large scale variation of the sample materials but merely the variation within the yet rather small original samples scanned. The samples used in the experiments are much larger and the results are therefore expected to better represent mean values (apart from possible systematic errors remaining). Nevertheless, the largest deviation between numerical and experimental results in these cases is less than 30%. This is of the same order of magnitude than the overall uncertainty inherent also in the used experimental method for thin samples.

TABLE 4.2 Numerical and experimental values of permeability in x, y and z directions (in physical units) for synthetic non-woven felt and hardwood paper sample. The numerical results obtained with LBM are given as mean values of results based on five non-overlapping subsamples, and the experimental results as mean values of five independent measurements with their standard deviation [Appendix II] [Geindreau et al., 2009].

Sample	Permeability k_{ii} [m^2· E -13]								
	k_{xx}			k_{yy}			k_{zz}		
	LBM	FDM	Experim.	LBM	FDM	Experim.	LBM	FDM	Experim.
Synthetic non-woven felt	290±10	352	311 ± 9	290±30	332	304 ± 9	270±30	305	270 ± 5
Hardwood paper	2.6±0.3	2.60	3.1 ± 0.1	2.7±0.3	2.84	3.1 ± 0.1	0.76±0.05	0.85	0.63 ± 0.01

Chapter 5

Permeability values of compressed fibre mats

In this chapter the experimental and numerical permeability analysis methods are applied for certain thin fibrous porous sample types (namely wet pressing felt, cardboard and newsprint) under mechanical stress. Finally in this section the permeability of different structural layers of the wet pressing felt are estimated numerically. Experimental measurements of the permeability values of individual layers are laborious or even unfeasible. The results and procedures presented in this section are applicable e.g. in finding the relevant material parameters for macroscopic models describing calandering, drying and wet pressing processes related to paper industry.

5.1 Comparison with model predictions and experimental results

Tomographic imaging of samples under compression

The geometries for the numerical analysis were again obtained utilising CXμT methods described in Sec. 4.2. In this case, however, the samples were scanned under static compression enabled by tubular sample holders with adjustable compression mechanism, see Fig. 5.1. The compression levels of the samples were selected to correspond to the thickness values during the experimental measurements.

Besides the fluid flow properties, the CXμT techniques allows direct analysis of also other relevant structural properties of the materials involved. For example, porosity of the sample was obtained from the thresholded subvolumes as the ratio of the number of pore voxels to the total number of voxels. Furthermore, comparison of tomographic reconstructions of samples at varying degree of compression shows that the volume of the solid phase remains approximately constant in uniaxial compression for the materials considered in this thesis. Using this result, a simple

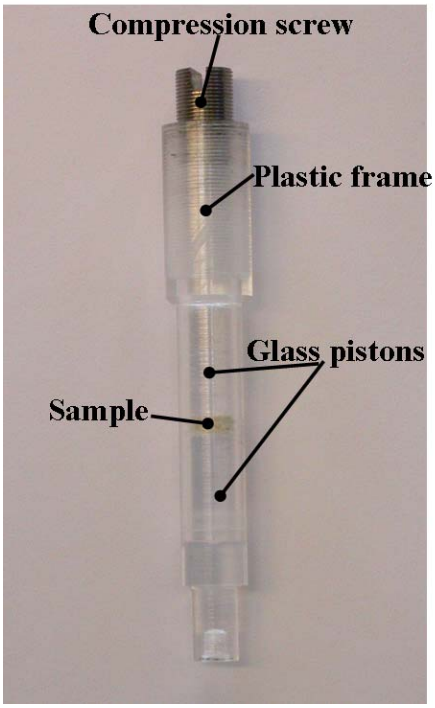

FIGURE 5.1 Tubular sample holder for tomographic imaging under static compression. During the scannings the samples were compressed between two polished class pistons inside tubular plastic frame. The compression levels were changed by adjusting the distance between the class pistons by compression screw.

relation between the porosity ϕ and thickness L_i of the sample is obtained:

$$\phi = 1 - \frac{(1-\phi_0)L_0}{L_i}, \tag{5.1}$$

where ϕ_0 and L_0 are the the porosity and the thickness of the sample obtained from the tomographic reconstruction in an arbitrary reference state, see Fig. 5.2.

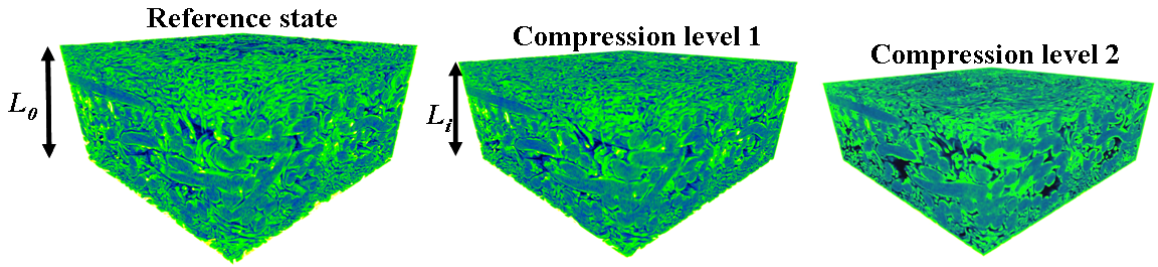

FIGURE 5.2 Visualisations of tomographic reconstructions of a wet pressing felt sample under different compression levels.

Numerical and experimental results

In Fig. 5.3 shown are the experimentally measured values of permeability coefficient as a function of porosity (calculated using Eq. 5.1) for plastic wet pressing felt (grammage W=1630 g/m^2 with original thickness of L_0=2.248 mm), cardboard made of chemical and mechanical pulp (W= 247 g/m^2, L_0= 0.412 mm) and soft nip calendered newsprint made of mechanical pulp (W= 52 g/m^2, L_0= 0.098 mm). Also shown are the corresponding results from LBM analysis. Four non-overlapping subvolumes from different locations of each tomographic reconstruction were used for numerical analysis. The error bars in the numerical results include the estimated statistical uncertainty due to the relatively small size of the samples that could be used in the analysis. The statistical uncertainty of the numerically solved values of permeability was thereby found to be less than $\pm$ 25 % for all sample types and under different compression levels. The maximum deviation of the measured and numerical values of permeability coefficient is less than 30 % including all cases. The results for the three different materials are in an order of magnitude agreement with earlier results for similar materials [Lindsay and Brady, 1993a, Lindsay and Brady, 1993b, Boerner and Orloff, 1994, Vomhoff et al., 2000].

The fitted curves based on equations by Happel, Kuwabara and Brundrett, Eqs (2.11), (2.12) and (2.17), are shown for the samples in Fig. 5.3. For all the cases, the Kozeny-Carman (not shown here) relation Eq. (2.9) gave results that were nearly identical with Happel formula Eq. (2.11). For the wet pressing felt sample, the Happel formula shows only marginal agreement with the data. One reason for this may be the highly inhomogeneous layered structure of the felt material. Nevertheless, the Happel formula allows for an order of magnitude comparison with the measured results: the radii of the two fibrous materials used in the present felt sample, i.e. the wire used in the woven base structure and the fine batt used in the surface layers, were analysed from the tomographic reconstructions, and found to be 115 μm and 30 μm, respectively. These are to be compared with fitted value 90 μm of the fibre radius r that appears in the Happel formula. For the cardboard sample, the Happel equation can not reproduce the measured data very well. However, the fitted value of the fibre radius r is 7 μm for the cardboard sample, which is quite close to the average wood fibre radius. For the wet pressing felt and the cardboard samples the Kuwabara correlation predict much lower decrease of permeability with decreasing porosity as compared to the measured values. However, the Brundrett correlation can be well fitted for both the wet pressing felt and the cardboard.

The newsprint data can be well fitted by the Kuwabara correlation. The fitted value of the fibre radius r that appears in the Kuwabara formula is 0.5 μm, which underestimates the radius of wood fibres but represents more likely the fines of the mechanical pulp. For the newsprint sample, the Happel and the Brundrett correlations are qualitatively distinct from the experimental and numerical data. They predict much stronger decrease of permeability with decreasing porosity as compared

to measured values. A plausible reason for this deviation is that the thin newsprint sample might include 'pinholes', i.e. more or less straight passages of flow through the sample that are not significantly constricted by compression. Consequently, it appears that the newsprint data can be well fitted by a modified Brundrett formula

$$k = m_1 \frac{\phi^2}{(1-\phi^2)} + m_2, \tag{5.2}$$

where m_2 is an another constant.

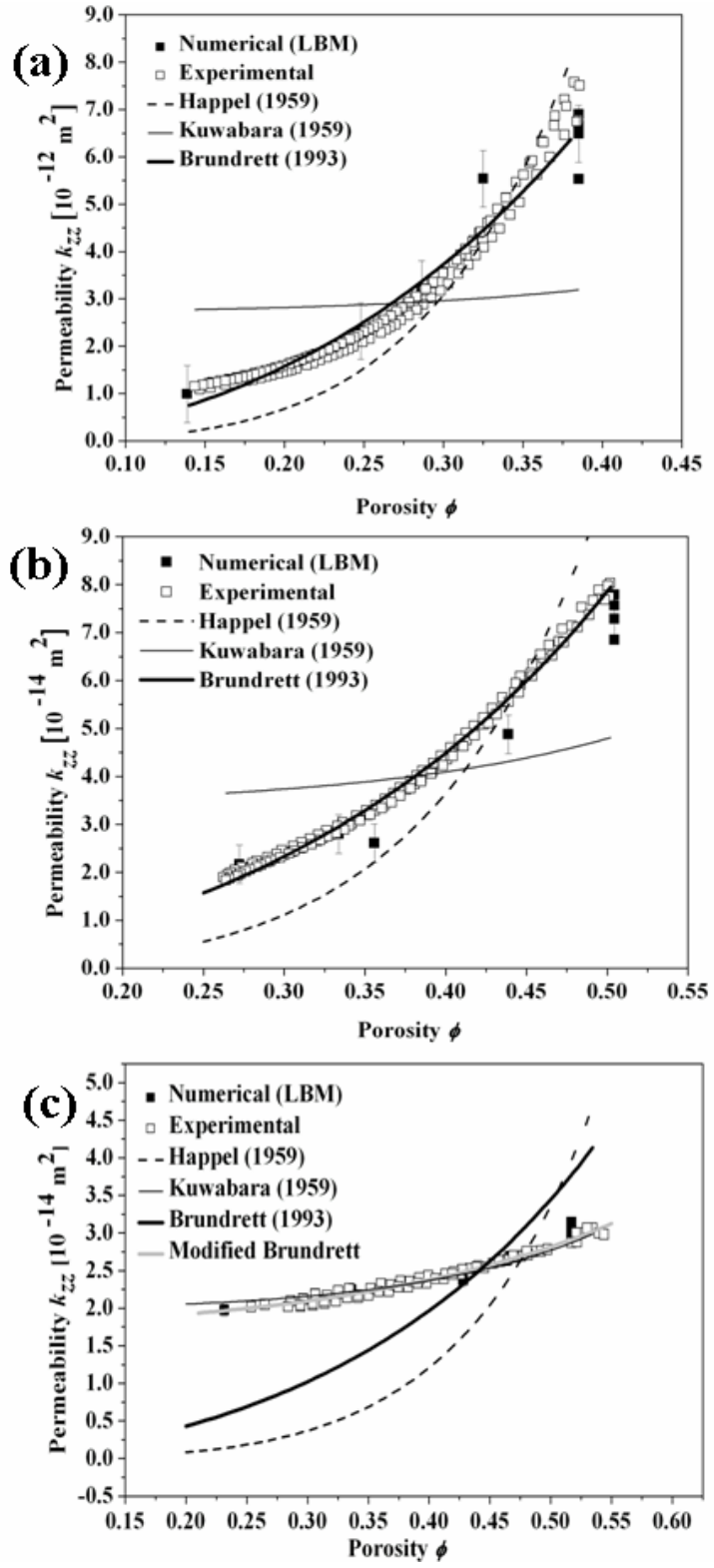

FIGURE 5.3 Numerical and experimental values of transverse permeability under various porosity levels with Happel (1959), Kuwabara (1959) and Brundrett (1993) fittings for (a) wet pressing felt, (b) cardboard and (c) newsprint samples [Appendix I]. The error bars of numerical results include the statistical variation due to small sample size estimated as the standard deviation for four independent subsamples (all the four results shown only for the highest porosity level). Experimental results are given for three similar samples. The total error of the experimental results is estimated to be less than 35 % (not shown).

5.2 Analysis of layered structures

The measured values of transverse permeability coefficient given in Sec. 5.1 were calculated by Darcy's law (Eq. (2.8)) using the total pressure difference over the entire thickness of the sample. These results (and the corresponding numerical values) thus represent effective mean values over the transverse dimension of the materials. The structure of the wet pressing felt studied here is layered, and the properties of the top and bottom layers may differ considerably from those of the middle layer. It is thus unclear, whether such effective mean values are actually useful if applied e.g. in modelling wet pressing [Roux and Vincent, 1991, El-Hosseiny, 1991, Kataja et al., 1992]. In wet pressing process paper web is compressed against the top layer of the felt, and the typical thickness of that layer is much larger than the thickness of the web. It thus appears that a proper description of fluid flow from the web into the felt requires knowing the properties of various layers of the felt separately and especially, the properties of the top layer next to the paper web. While a direct measurement of e.g. permeability of various layers of a pressing felt might be quite tedious, the present method based on tomographic imaging and numerical flow solution provides a straightforward means for such evaluation. For this part of the work, a wet pressing felt sample with grammage 1630 g/m^2 and original (not compressed) thickness 2.44 mm was studied.

Image analysis

The regions of different kinds of fibres in the triple-layered structure of the present wet pressing felt overlap; the concept of a layer is, to certain extend, a matter of definition (see visualisation of the 2D slices of tomographic reconstructions in Fig. 5.4). Here the layers are defined by means of the distribution of average fibre diameter in the transverse direction. Fig. 5.5 shows such distributions found by the maximal sphere filling algorithm applied on the solid phase in binarised tomographic reconstructions of the sample scanned at two levels of compression. The middle layer is clearly visible as a plateau of fibres with relatively high value of mean diameter. The positions of the boundaries between the layers are defined as locations where the average fibre diameter has the value half-way between the typical values at the middle and surface layers. The same criterion for the layers is used for all states of compression. It was verified by visual inspection, that the layers specified in this manner indeed include closely the same fibre material points in tomographic images corresponding to different levels of compression. It thus seems justified to compare the results obtained for each individual layer under varying degree of compression.

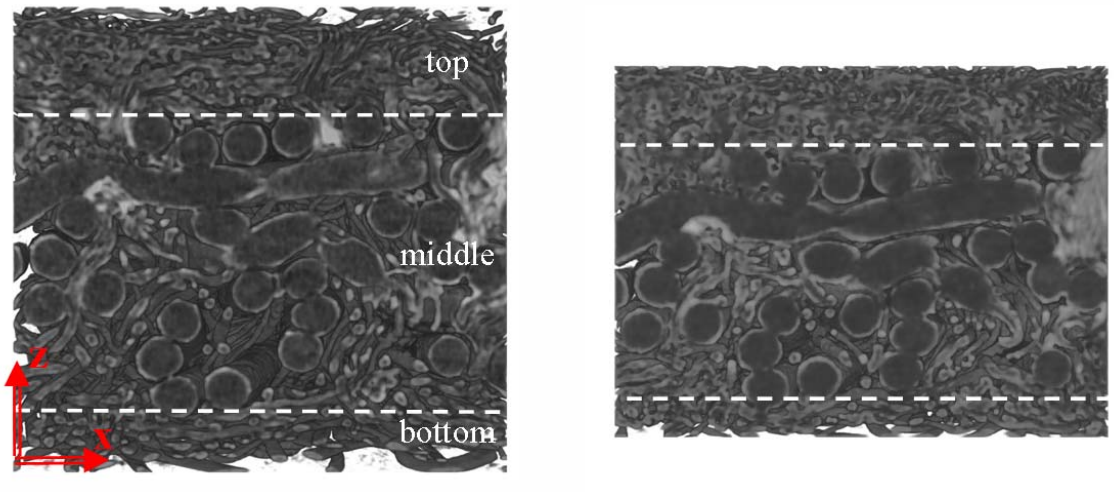

FIGURE 5.4 2D slices of tomographic reconstructions of the wet pressing felt sample in two different states of compression. Also shown are the top, middle and bottom layers as specified in Fig. 5.5 [Appendix II]

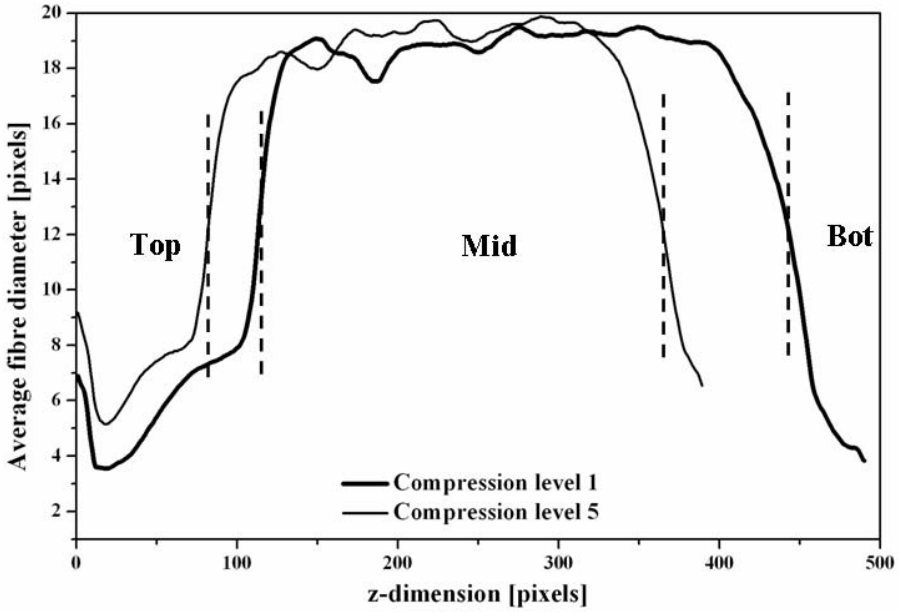

FIGURE 5.5 Distribution of mean fibre diameter in transverse direction in two states of compression of the wet pressing felt sample. The vertical dashed lines indicate positions of boundaries between the top, middle and bottom layers of the felt [Appendix II].

Transverse flow permeability

The numerically analysed dependence of compression (thickness of the entire felt sample) on transverse permeability coefficients k_{zz} for the three layers of the wet pressing felt are presented in Fig. 5.6a. The mean permeability values for the entire thickness of the sample determined numerically and experimentally is also presented. In Fig. 5.6b shown is the same data but plotted for each layer as a function of porosity of the layer. The mean permeability results are plotted as a function of porosity of the entire sample. The values of porosity were calculated using Eq. (5.1). Numerical analyses have been made using LBM for several subsamples in the cases of the highest porosity values and for a single subsample in all other cases.

The transverse permeability of the top layer is, as expected, lower than the permeability of the middle layer. This is simply due to higher specific surface of the fine batt fibres in the top layer. Instead, the transverse permeability of the bottom layer at a given degree of compression is much higher than that of the top and middle layers. This is explained partly by the higher porosity of the bottom layer, as shown in Fig. 5.6b, and partly by the fact that the bottom layer is very thin. Obviously, it includes open flow channels through the entire layer. This results in a higher value of flow permeability than that of a corresponding bulk material.

Comparing the results shown in Fig. 5.6 indicates that the behaviour of the mean permeability of the entire sample differs significantly from that of individual layers. For the present wet pressing felt sample, the transverse permeability of the top layer is smaller than the mean transverse permeability by a factor of 2–3 in the range of overall compression studied here. Clearly, such a difference should be taken into account e.g. in numerical analysis of water removal in wet pressing process.

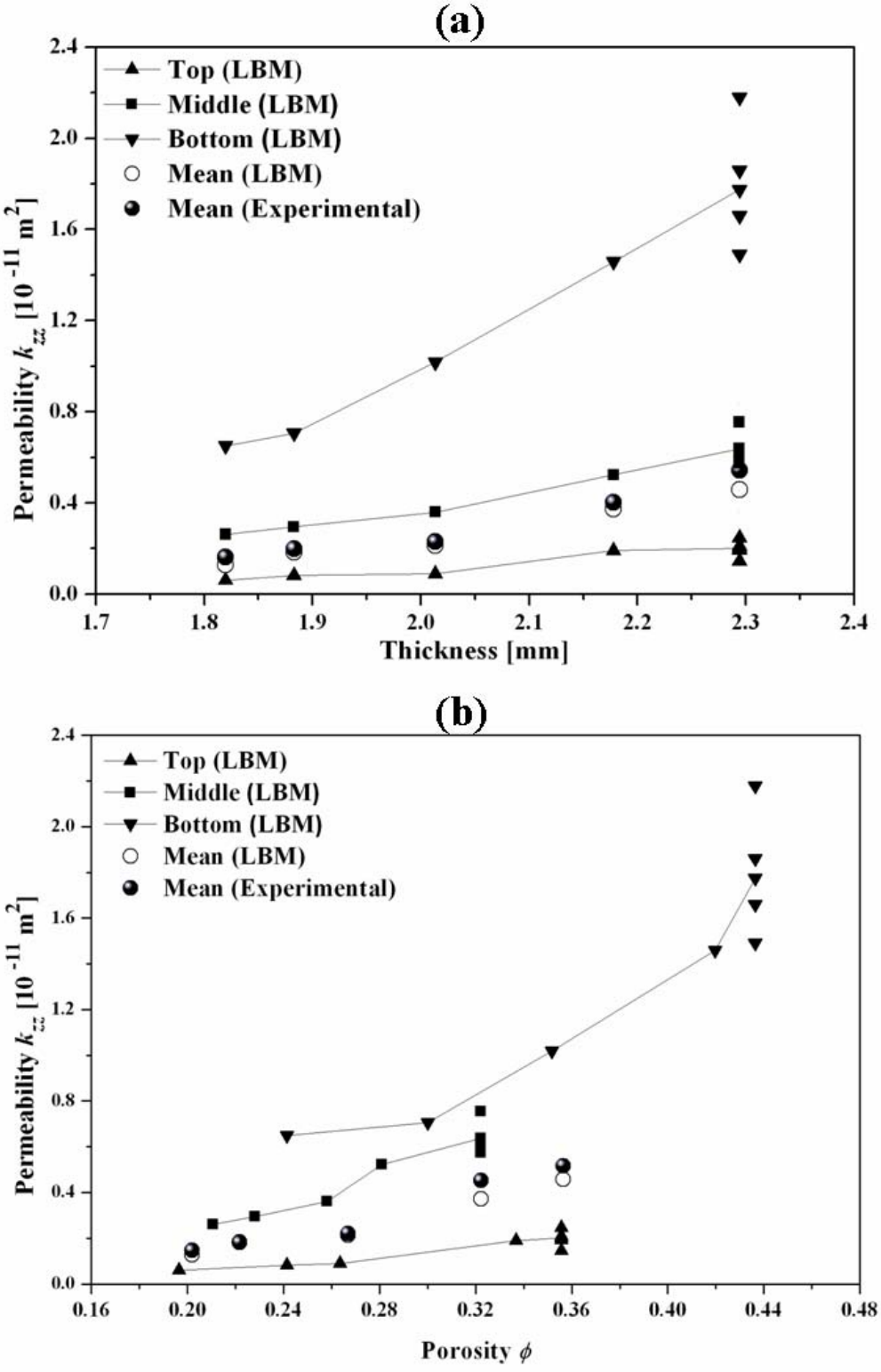

FIGURE 5.6 Numerical values of transverse permeability for top, middle and bottom layers of the wet pressing felt as a function of thickness of the entire sample (a) and as a function of porosity measured separately for each layers (b). In (a) and (b) given are also the experimental and numerical values of mean permeability for the entire sample. Numerical analyses have been made for five subsamples in the cases of the highest thickness/porosity value in order to estimate the statistical variation of the results [Appendix II].

In-plane flow permeability

The in-plane permeability coefficients k_{xx} for the three layers of the wet pressing felt as a function of the entire sample thickness are shown in Fig. 5.7a. Also shown is the mean permeability for the entire sample determined by LBM and by experimental measurements. In Fig. 5.7b shown is the same data but plotted for each layer as a function of porosity of the layer. The mean values of permeability are plotted as a function of the porosity of the entire sample. Numerical analyses have been made using LBM for several subsamples in the cases of the highest porosity values and for a single subsample in all other cases. The in-plane permeability values are also obtained by FDM for the lowest compression levels [Geindreau et al., 2009].

The in-plane permeability of the top and bottom layers fall approximately on the same curve when plotted as a function of porosity. This is as expected since the radius, and thus the specific surface of fibres in these surface layers is nearly the same (and there is no channelling effect present in the lateral flow direction). For the wet pressing felt sample, the in-plane permeability of the top layer is smaller than the mean in-plane permeability by a factor of 2-3 in the range of overall compression studied here.

The results presented in the Sec. 5.2 and the Figs 5.7a and 5.7b demonstrate clearly the advantage of the combination of numerical methods with CXμT for analysing permeability values of complex materials. The experimental measurement techniques are applicable only for measuring the mean permeability values and are not suitable for detailed analysis of single layers.

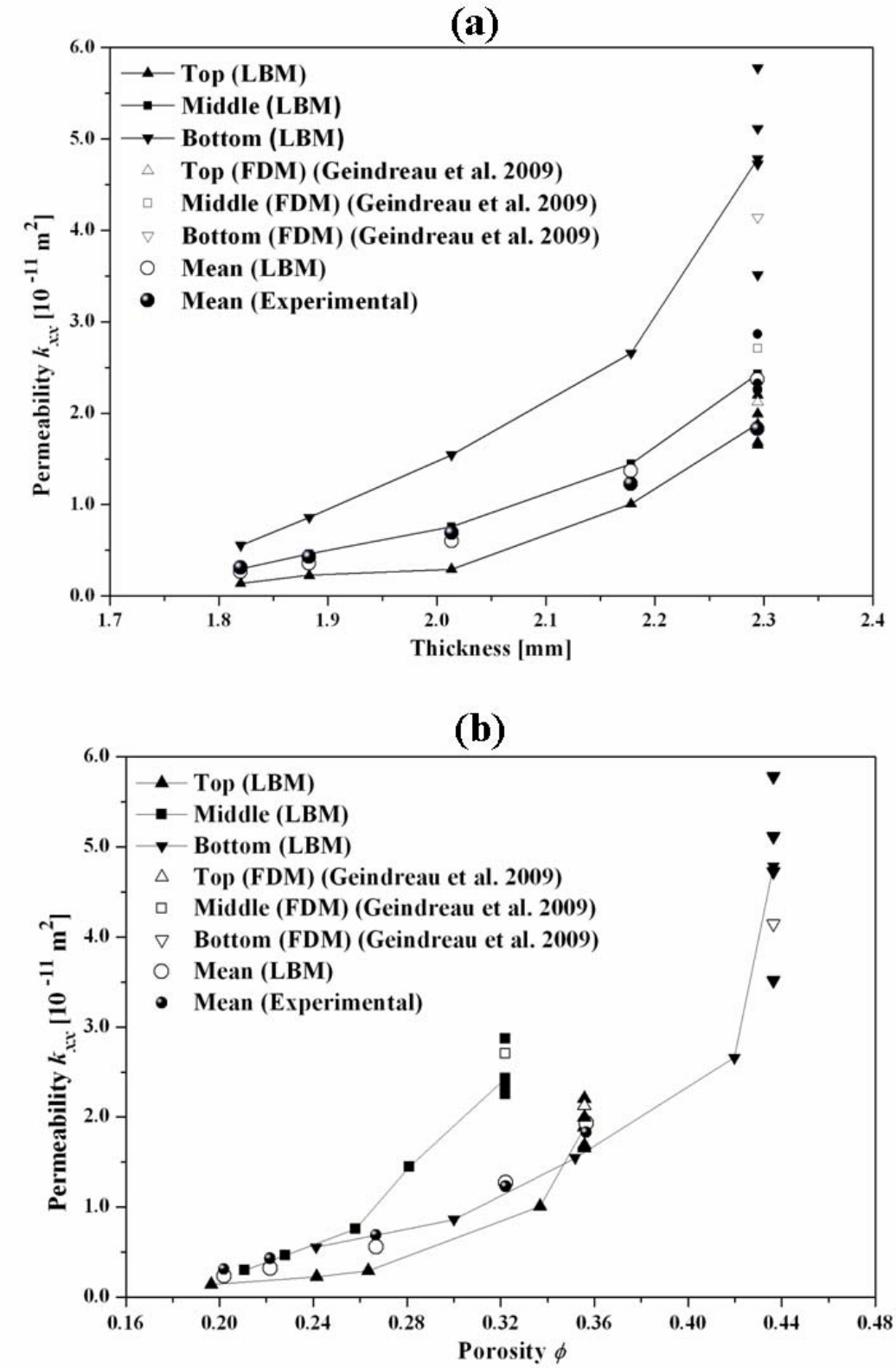

FIGURE 5.7 Numerical values of in-plane permeability for top, middle and bottom layers of the wet pressing felt as a function of thickness of the entire sample (a) and as a function of porosity measured separately for each layers(b). In (a) and (b) given are also the experimental and numerical values of mean permeability for the entire sample and the FDM results for the lowest compression levels. Numerical LBM analyses have been made for five subsamples in the cases of the highest thickness/porosity value in order to estimate the statistical variation of the results [Appendix II].

Chapter 6

Structure and imbibition

Imbibition in porous heterogeneous materials is a complicated process due to the complex internal micro-scale structures of the media. During the last century, the phenomena related to the imbibition process have been investigated by various methods, see e.g. Refs [Lucas, 1918,Washburn, 1921a,Washburn, 1921b,Dullien et al., 1977, Bear, 1972, Dullien, 1979, Lenormand and Zarcone, 1984, Coles et al., 1998, Senden et al., 2007, Turian and Kessler, 2000, Dube et al., 2000, Erickson et al., 2002, Bico and Quéré, 2004, Mélean et al., 2003, von Bahr et al., 2004, Roberts et al., 2003, Alava et al., 2004, Dube et al., 2007, Fabritius, 2007, Hyväluoma, 2009]. Some of these recent studies are based on CXμT techniques. In this part of the work, tomographic reconstructions are combined to a void space segmentation analysis for studying structural characteristics of pore structure and their relation to imbibition process. The utilisation of the methods is demonstrated by running the analyses for a series of tomographic reconstructions of porous heterogeneous materials, namely liquid packaging boards. Values of their water absorption coefficient (introduced by Benavente et al. [Benavente et al., 2002]) are obtained utilising the void space segmentation analysis in combination with CXμT reconstructions. These values are compared with experimentally measured results. Also the permeability results obtained by the numerical lattice Boltzmann analysis are compared with experimentally measured permeability values. In this part of the work, the experimental permeability values are obtained from dynamic imbibition measurements.

6.1 Spontaneous imbibition

In Fig. 6.1 is a schematic illustration of a measurement set-up where a strip of a porous heterogeneous sample is placed in contact with wetting liquid and spontaneous imbibition occurs. The liquid front velocity during imbibition process in a porous sample can be written using Darcy's law Eq. (2.5) [Alava et al., 2004]

$$U = \frac{dH}{dt} = \frac{1}{\phi}\frac{k}{\mu}\frac{\Delta p}{H}, \tag{6.1}$$

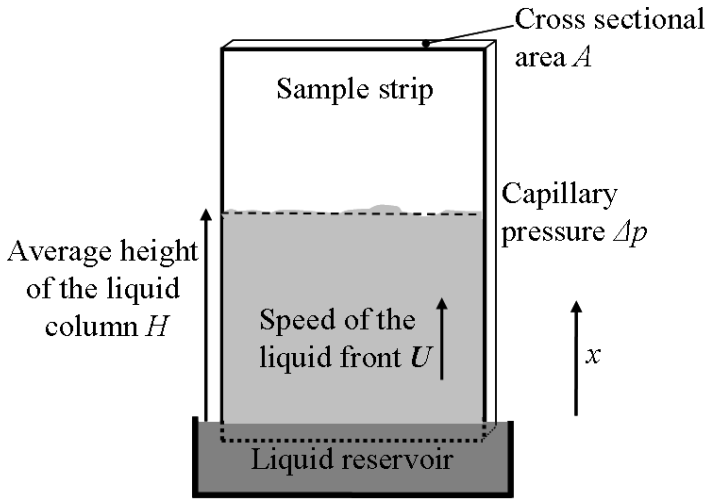

FIGURE 6.1 A schematic illustration of imbibition process in a porous sample strip [Appedix IV].

where ϕ is the porosity of the material, k is the permeability coefficient, μ is the dynamic viscosity of the fluid, H is the average height of the liquid front and Δp is the capillary pressure.

Simple model for porous material consists of straight cylindrical capillaries with radius a. The capillaries form an angle α with x direction, see Fig. 6.1. The azimuthal angle of the capillaries is randomly distributed. The permeability coefficient for Poiseuille flow in such a capillary system is given by

$$k = \frac{\phi a^2}{8\tau}, \tag{6.2}$$

where $\tau = 1/(cos\alpha)^2$. Using capillary pressure $\Delta p = (2\gamma \cos\theta)/a$ together with Eqs (6.1) and (6.2), the mass of the imbibed liquid per cross sectional area of the sample can be solved. The result is

$$\frac{\Delta M}{A} = \phi\rho H = \phi\rho\sqrt{\frac{a\gamma cos\theta}{2\tau\mu}}\sqrt{t} = C\sqrt{t}, \tag{6.3}$$

where ρ is the density of the fluid, γ is the surface tension, θ is the contact angle, t is time and C is the so-called water absorption coefficient [Benavente et al., 2002].

Although derived assuming a simple capillary model, Eq. (6.3) can be applied to many porous materials by replacing τ with tortuosity of flow paths (see Eq. (2.10)) and radius of the capillaries e.g. by the mean hydraulic radius $r_h = A_p/l_p$, where A_p is the cross sectional area and l_p is the perimeter of the pore channel. As demonstrated below, the structural parameters ϕ, r_h and τ contained in the water absorption coefficient can be estimated directly from tomographic reconstructions

of porous samples by utilising suitable 3D image analysis tools.

6.2 Demonstration samples and their properties

Sample preparation

Three distinct series of unsized (hydrophilic) and chemically identical cardboards used in liquid packaging board production were prepared in laboratory conditions. Laboratory sheets with grammage close to 250 g/m^2 were prepared from refined and unrefined bleached ECF softwood pulp using a dynamic Formette paper sheet former. The refining degrees of the refined and "unrefined" pulps were 35 SR (Schopper Riegler number) and 15 SR, respectively. Different press loads were used to obtain high and low density sheets. The aim of the different manufacturing procedures was to produce dissimilar pore structures for testing and demonstration purposes. The demonstration sample types are hereinafter identified by names Ref1, Ref2 and Ref3. Samples Ref1 and Ref3 were prepared from the unrefined pulp and sample Ref2 from the refined pulp. Sample Ref3 had the lowest pressing load. Visualisations of tomographic reconstructions of the samples are shown in Fig. 6.2. The difference between the samples Ref1 and Ref2 is the higher refining degree of sample Ref2. Structural details of the samples are listed in Table 6.1.

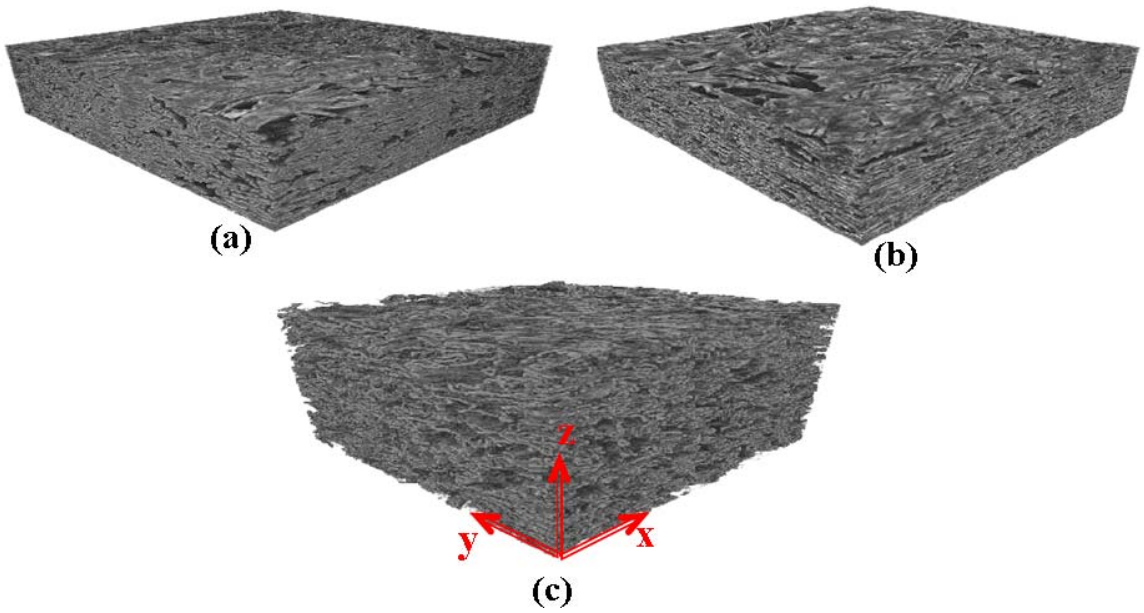

FIGURE 6.2 Tomographic reconstructions of the demonstration samples: (a) Ref1, (b) Ref2 and (c) Ref3. Physical dimensions of the visualised sample geometries are (x, y and z) 700 μm x 700 μm x thickness of the subvolumes. The thickness values of the subvolumes are 260 μm, 260 μm and 520 μm for Ref1, Ref2 and Ref3, respectively [Appendix IV].

TABLE 6.1 Porosity, thickness, grammage and density values of the demonstration samples [Appendix IV].

Sample id	Porosity [%]	Thickness [µm]	Grammage [g/m²]	Bulk density [kg/m³]
Ref1	29.1 ± 0.1	258 ± 9.7	245 ± 0.70	926 ± 5
Ref2	29.5 ± 0.1	271 ± 12.8	249 ± 1.88	919 ± 5
Ref3	55.9 ± 0.1	529 ± 18.8	250 ± 1.88	500 ± 5

Void space segmentation analysis and pore size distribution

Micro-scale structures of the demonstration samples are obtained by a void space segmentation analysis (VSSA). In the beginning of the VSSA the whole pore structures in tomographic subvolumes (see Fig. 6.2) are divided to individual pores by a watershed based segmentation algorithm [Berry and Burnell, 2001]. A single pore is assumed to be connected to the neighbouring pores by local narrowings, i.e. throats. Segmentation to individual pores is realised by fitting spheres into the whole void space. The throats are defined as a local minimum of the radii of fitted spheres. Fitting of spheres is performed in 3D, thus the throats are detected in all directions and shapes. After locating the throats, the void space is divided to individual pores. A schematic illustration of three neighbouring pores in the pore network is shown in Fig. 6.3. Thus, in order to increase the image noise tolerance, isolated solid objects in the void space of the reconstructions are allowed inside the fitted spheres. The segmented void spaces can be used for analysing the pore and throat size distributions. Image moments [Gonzalez and Woods, 2002] are utilised to calculate volumes, centres of mass and principal axes of the identified pores. The graph structures obtained by the image moments include nodes representing the centres of mass of each pore and lines connecting the neighbouring ones, i.e. chords presented in Fig. 6.3. Furthermore, the information related to orientation and length of the chords, is used for analysing fluid flow tortuosity τ through the void space. Line segments describe the average dimensions of void channels to a certain direction. A few line segments are sketched in the y-direction in the Fig. 6.3.

The pore radius distributions given by the VSSA were compared with experimental mercury intrusion porosimetry results. Modes and medians of the distributions for each demonstration sample types are listed in Table 6.2. The methods gave qualitatively similar distributions. Also the differences between the sample types were found explicitly with both the methods. The VSSA combined to CXμT was observed to be suitable for structural characterisation and comparison purposes. By utilising the VSSA it is possible to characterise structural details of a porous material within the tomographic imaging resolution precision.

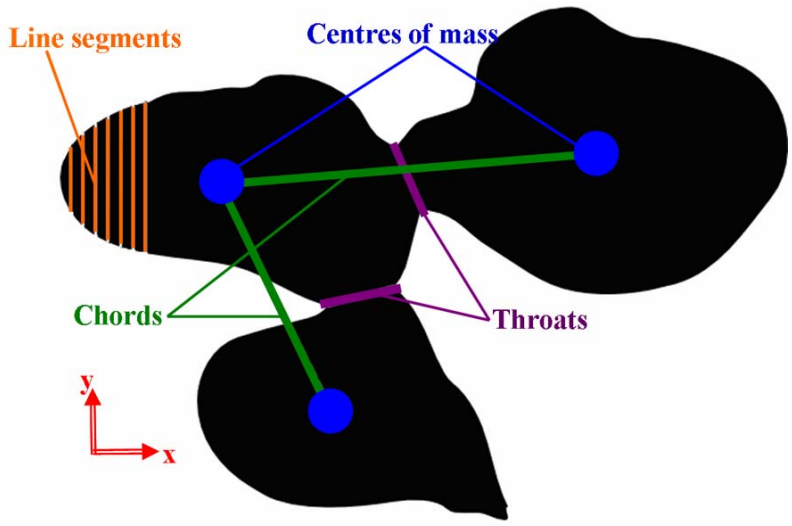

FIGURE 6.3 A sketch of three neighbouring pores separated by the VSSA. Centres of mass, chords, pore throats, and line segments are identified. The void space is illustrated black [Appendix IV].

TABLE 6.2 The VSSA combined to tomographic reconstructions and mercury (Hg) intrusion porosimetry values for modes and medians of the pore radius distributions Image analysis results are given as mean values of the three analysed subvolumes per sample type. Statistical uncertainty of the image analysis results is ± 20 %. Hg results are given for one measured sample strip with dimension of 50 mm x 50 mm [Appendix IV].

Sample id	Mode [µm] Tomography / Hg	Median [µm] Tomography / Hg
Ref1	2.0 / 1.6	4.0 / 2.8
Ref2	2.0 / 1.6	3.5 / 2.3
Ref3	5.3 / 7.0	6.5 / 6.5

In-plane permeability

Experimentally determined in-plane imbibition speeds as a function of liquid column heights for imbibition processes in x and y directions are shown in the Fig. 6.4. Experimental measurements were conducted for sample strips with dimensions of 40 mm x 150 mm, the long side being parallel to the imbibition direction, see schematic illustration of the measurement set-up in Fig. 6.1. Dynamic imbibition experiments were conducted by ion-changed water solution of (30 % in mass) potassium iodine and blue litmus colour. Permeability is estimated (by utilising equation Eq. (6.1)) from the fitted curves

$$U = f_p \frac{1}{H}, \tag{6.4}$$

TABLE 6.3 Experimental and numerical permeabilities. Numerical LBM results are given as mean values of three independent subvolumes per sample type. Statistical variation of the numerical results is ± 20 % [Appendix IV].

Sample id	$k_{xx}/k_{yy}[m^2 \cdot E\text{-}13]$ Exp.	$k_{xx}/k_{yy}[m^2 \cdot E\text{-}13]$ LBM
Ref1	1.09 / 1.08	1.14 / 0.854
Ref2	0.495 / 0.488	0.748 / 0.459
Ref3	4.46 / 4.44	27.3 / 20.3

where f_p is a fitting parameter (see Fig. 6.4). Permeability is calculated from the experimental data using constant capillary pressure, constant median pore radius value (see Table 6.2) and constant porosity (see Table 6.1). The experimentally measured values for the surface tension, viscosity and contact angle were γ = 0.072 kg / s^2, μ = 0.001 (kg m)/s and $\theta = 9°$, respectively [Appendix IV].

Numerical lattice Boltzmann permeability analyses were conducted for three independent tomographic subvolumes of each sample types. Numerical LBM and experimental permeability results for the demonstration samples are listed in table 6.3. Factors between the experimentally determined permeability values and numerical LBM results vary for samples Ref1 and Ref2 between 1.05–1.51. For the sample Ref3 the difference between the experimental and numerical results is higher. The deviation between the results may be at least partly explained by swelling effects of the fiber structure due to wetting liquid. Also gravity can influence the experimental results. In the numerical analysis the gravity and swelling effects are not included. The limited resolution of the tomographic reconstruction may also cause uncertainty in the numerical results.

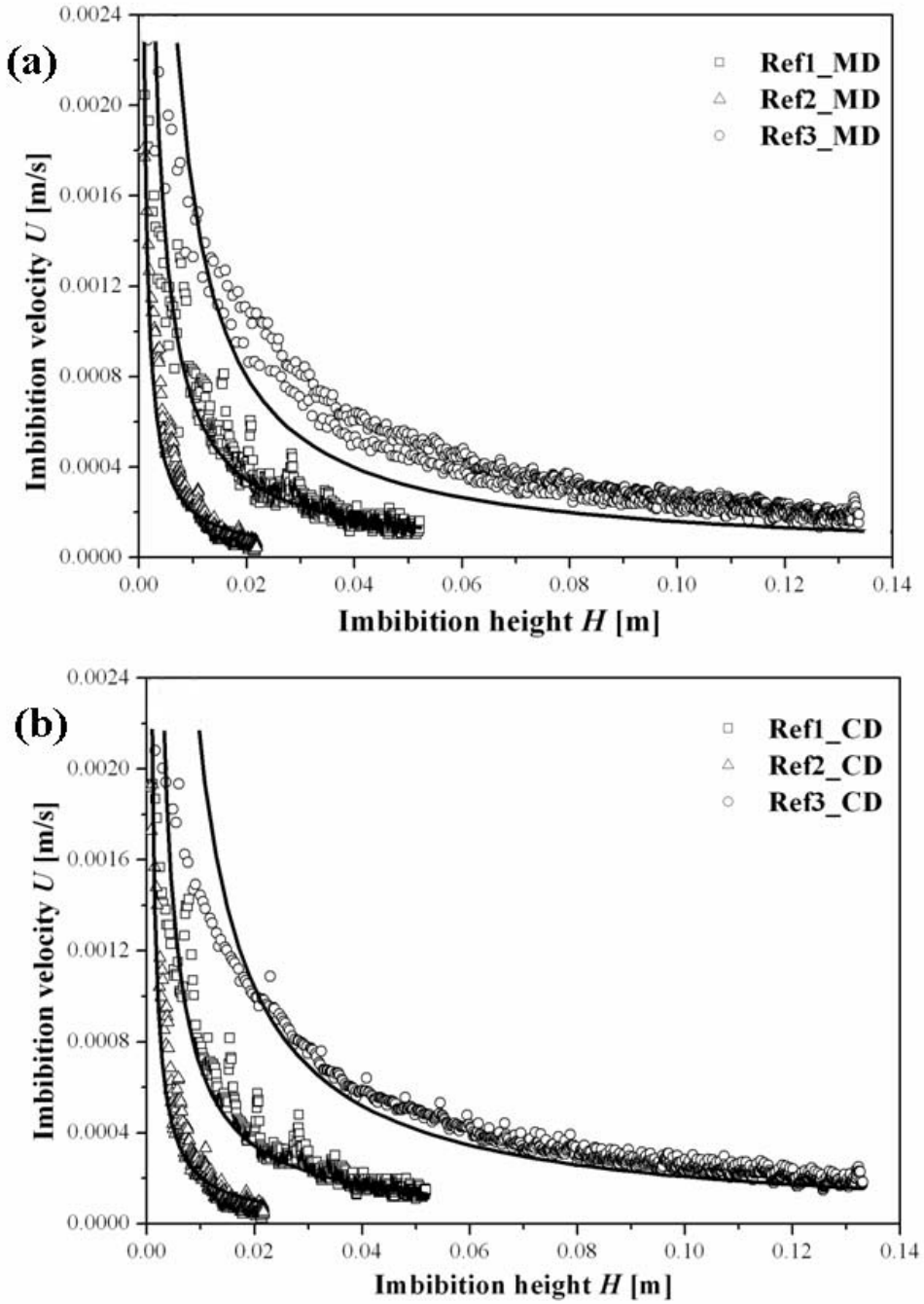

FIGURE 6.4 Experimentally measured imbibition speed as a function of imbibition height for imbibition processes in (a) x and (b) y directions [Appendix IV].

Water absorption coefficient

Water absorption coefficients (in Eq. (6.3)) of the demonstration samples were measured experimentally and by characterising the structural properties (ϕ, r_h and τ) utilising the VSSA. Porosities of the samples were obtained from thresholded subvolumes as the ratio of the number of void voxels to the total number of voxels. Pore throat sizes were estimated from pore throat size distributions as median values. Hydraulic radii of pore channels were estimated as ratio between the area and the perimeter of the pores. Tortuosity values were analysed from the chord structure obtained by the VSSA as ratio between the sum of lengths and the sum of length projections to analysed direction. Contact angle θ and liquid properties ρ, μ and γ of the (ion-changed water, potassium iodine and blue litmus colour) solution were measured. These results were utilised for calculating the VSSA -based water absorption coefficient, θ = 9°, ρ = 1280 kg/m^3, μ = 0.001 (kg m)/s and γ = 0.072 kg / s^2.

The water absorption coefficients measured experimentally and estimated from tomographic reconstructions utilising the VSSA for the demonstration samples are listed in Table 6.4. The experimental and image analysis results are in good agreement. The maximum difference between the results is 40 %. The difference between the results may be explained by swelling effects of the fiber structure due to wetting liquid or influence of gravity. Also limited resolution of the tomographic reconstructions may cause uncertainty for the numerical results. The sample type Ref3 has the highest water absorption coefficient due to the highest porosity level. The water absorption coefficient of the sample Ref1 is on average 45 % higher than of the sample Ref2. This is due to higher refining degree of the sample type Ref2. Compared to the sample Ref1, the pore structure of the sample Ref2 is more complex and fine-structured.

The analyses presented in this chapter demonstrate the utilisation of the combination of CXμT and image analysis methods for studying connections between the characteristics of pore structure and imbibition properties. The advantage of the combination of CXμT and the VSSA is that the structural characteristics of a

TABLE 6.4 Water absorption coefficients measured experimentally and estimated from tomographic reconstructions utilising the VSSA. Image analysis results are given as mean values of three independent subvolumes. Statistical uncertainty of the image analysis results is ± 20 % [Appendix IV].

Sample id	φ [%]	r_h (x / y) [µm]	τ (x / y)	C_{VSSA} (x / y) [kg/(m^2 · s$^{1/2}$)]	C_{exp} (x / y) [kg/(m^2 · s$^{1/2}$)]
Ref1	29.5	2.21 / 2.26	1.80 / 2.43	2.40 / 2.09	1.74 / 1.63
Ref2	29.1	1.03 / 1.11	1.82 / 2.28	1.67 / 1.50	1.24 / 1.06
Ref3	55.9	2.65 / 2.65	1.80 / 2.10	5.00 / 4.62	4.62 / 4.51

porous heterogeneous materials can be analysed straight from tomographic reconstructions. This information can readily be utilised for predicting the fluid flow properties of a porous heterogeneous material without solving the actual fluid flow numerically, experimentally or analytically. However, advanced statistical analysis is further required to establish the reliability of the results obtained by the VSSA.

Chapter 7

Conclusions and Outlook

The objective of this thesis was to find out if it is possible to numerically model fluid flow in realistic porous materials and to obtain results that agree quatitatively with experimental data. To this end, numerical and experimental methods for analysing fluid flow properties of porous materials were developed. Combination of a numerical lattice Boltzmann method and micro-tomographic reconstructions was utilised for analysing fluid flow permeability through porous media. Special attention was paid for producing realistic computational grids for the numerical permeability analysis utilising high-resolution tomographic imaging and advanced image processing methods. A major potential source of uncertainty within the approach of using a numerical method in combination with tomographic reconstruction is the numerical error caused by the finite resolution of the numerical grid used. The discretisation error was estimated solving fluid flow through numerical grids of different sizes and the resulting values of permeability coefficient were compared with analytically solved values. The discretisation error for the fibrous materials analysed in this thesis was estimated to be less than 10%.

The results obtained by the numerical lattice Boltzmann method were verified in several ways. First, by analysing permeability values of various rod geometries and comparing the results with the corresponding analytical values and to the numerical values solved by finite-difference and finite-element methods. Second, the numerical lattice Boltzmann permeability values for realistic fibrous materials were compared with the results obtained by finite-difference method. Finally, the numerical permeability values were compared with experimental results. To this end, a measurement device and a procedure for measuring the Darcian permeability coefficient of compressible porous materials was developed and tested. The method was designed to be especially suitable for measuring thin sheet-like samples. The construction of the permeability measurement apparatus, the experimental procedure used and the data processing were all designed in the purpose of minimising the known sources of uncertainty. Estimate for the maximum total errors for the transversal and in-plane permeability results are 35% and 20%, respectively. The

device was applied for measuring the dependence of transverse and in-plane flow permeability for air on the degree of compression for different materials, namely wet pressing felt, cardboard and newsprint.

The methods based on tomographic imaging and numerical methods for solving fluid flow properties in porous heterogeneous materials was tested to be suitable procedure for evaluating permeability of porous heterogeneous samples under various compression levels. Permeability values of various compressed fibre mats were evaluated under compression and decreasing porosity level by both the experimental and the numerical methods. The results were found to be in close agreement, regarding the absolute values of permeability, and its dependence on porosity (degree of compression) of the materials. Numerical permeability analysis was applied in evaluating the transverse and in-plane permeability separately for top, middle and bottom layers of the layer-structured wet pressing felt. This application demonstrates the potential of utilising tomographic reconstructions and numerical analysis methods for solving fluid flow in porous materials. Obtaining such detailed and new information on material properties would be very difficult to obtain e.g. by direct experiments.

Methods combining CXμT and image analysis for studying correlations between internal pore geometry and imbibition process in porous heterogeneous materials was developed. The usefulness of the image analysis methods was demonstrated by estimating the water absorption coefficients of three differently manufactured liquid packaging boards. Water absorption coefficients of same materials were also measured experimentally and the results were found to be in good agreement with those obtained from 3D tomographic image analysis. In addition, permeability of the samples was determined both by experimental imbibition measurements and by numerically utilising the lattice Boltzmann method in combination with x-ray tomographic reconstructions. The experimental and numerical permeability values were again in good agreement.

To conclude, the developed analysis methods provide an efficient combination of tools for analysing the structural details and dynamic properties of existing materials and even for designing new ones. The methods can lead to new insight into 3D fluid flow properties in porous heterogeneous materials. As recommendations for future work could be structural and fluid flow analyses of wet fibre webs. Flow properties through wet fibre webs differ from the properties of dry samples. The differences arise from the changes in the fibre structure (e.g. swelling of the fibres), the portion of such pores which are not accessible for water flow and other flow effects. The preceding characteristics and much more could be analysed from tomographic reconstructions of wet samples utilising image processing and numerical analysis tools. Perhaps in the near future, the development of tomographic imaging applications reveal the structure of wet fibre webs and thus facilitate the detailed analyses related to many practical processes.

Bibliography

[Aaltosalmi et al., 2004] Aaltosalmi, U., Kataja, M., Koponen, A., Timonen, J., Goel, A., Lee, G., and Ramaswamy, S. (2004). Numerical analysis of fluid flow through fibrous porous materials. *J. Pulp Paper Sci.*, 30(9):251–255.

[Abraham et al., 2000] Abraham, G. T., Daoud, W. Z., and Renken, K. J. (2000). Experimental measurements on the permeability coefficient of a concrete sample under low pressure differences. *Int. Radon Symp.*, pages 12.0–12.12.

[Adler, 1992] Adler, P. M. (1992). *Porous Media, Geometry and Transport*. Butterworth-Heinemann, Stoneham.

[Alaraudanjoki, 2008] Alaraudanjoki, J. (2008). Private communication.

[Alava et al., 2004] Alava, M., Dube, M., and Rost, M. (2004). Imbibition in disordered media. *Adv. Phys.*, 53:83–175.

[Andersson et al., 2009] Andersson, A. G., Westerberg, L. G., Papathanasiou, T. D., and Lundström, T. S. (2009). Flow through a two-scale porosity material. *Res. Lett. Mat. Sci.*, page 701512.

[Annand, 1952] Annand, W. J. D. (1952). The resistance to air flow of wire gauzes. *J. Royal Aeronautical Soc.*, 57:141–146.

[Arns et al., 2004] Arns, C. H., Knackstedt, M. A., Pinczewski, W. V., and Martys, N. S. (2004). Virtual permeametry on microtomographic images. *J. Petroleum Sci. Eng.*, 45:41–46.

[Bear, 1972] Bear, J. (1972). *Dynamics of Fluid in Porous Media*, pages 151–173. Dover Publications inc.

[Belov et al., 2004] Belov, E. B., Lomov, S. V., Verpoest, I., Peters, T., Roose, D., Parnas, R. S., Hoes, K., and Sol, H. (2004). Modelling of permeability of textile reinforcements: lattice boltzmann method. *Composites sci. tech.*, 64:1069–1080.

[Benavente et al., 2002] Benavente, D., Lock, P., del Cura, M. Á. G., and Ordór ez, S. (2002). Predicting the capillary imbibition of porous rocks from microstructure. *Trans. Por. Media*, 49(1):59–71.

[Berry and Burnell, 2001] Berry, R. and Burnell, J. (2001). *The Handbook of Astronomical Image Processing*, pages 13–17, 194. Willmann-Bell, USA.

[Bhatnagar et al., 1954] Bhatnagar, P. L., Gross, E. P., and Krook, M. (1954). A model for collision processes in gases. i. small amplitude processes in charged and neutral one-component systems. *Phys Rev.*, 94(3):511–525.

[Bico and Quéré, 2004] Bico, J. and Quéré, D. (2004). Precursors of impregnation. *J. Pulp Paper Sci.*, 62(3):348–353.

[Boerner and Orloff, 1994] Boerner, J. and Orloff, D. (1994). The effect of basis weight and freeness on sheet permeability and critical impulse drying temperature. *Tappi J.*, 77(2):163–168.

[Brundrett, 1993] Brundrett, E. (1993). Prediction of pressure drop for incompressible flow through screens, journal of fluids engineering. *J. Fluid Eng.*, 115(2):239–242.

[Buldyrev et al., 1992] Buldyrev, S. V., Barabási, A. L., Caserta, F., Havlin, S., Stanley, H. E., and Vicsek, T. (1992). Anomalous interface roughening in porous media: Experiment and model. *Phys. Rev. A.*, 45:R8313.

[Carlsson et al., 1983] Carlsson, G., Lindström, T., and Florén, F. (1983). Permeability to water of compressed pulp fiber mats. *Svensk papperstidning*, 86(12):R128–R134.

[Ceckler and Thompson, 1982] Ceckler, W. H. and Thompson, E. V. (1982). Wet pressing. Final report of Wet Pressing Project 1, University of Maine, Orono.

[Chen, 1982] Chen, F. J. (1982). *The Permability of Compressed Fiber Mats and the Effects of Surface Area Reduction and Fiber Geometry*. Ph.D. Thesis, The Institute of Paper Science and Technology, Atlanta, Georgia.

[Coles et al., 1998] Coles, M. E., D. Hazlett, R., P. Spanne, E. Soll, W., and and Jones, E. L. K. W. (1998). Pore level imaging of fluid transport using synchrotron x-ray microtomography. *J. Petroleum Sci. Eng*, 19(1):55–63.

[Czél and Czigány, 2008] Czél, G. and Czigány, T. (2008). A study of water absorption and mechanical properties of glass fiber/polyester composite pipes -effects of specimen geometry and preparation. *J. Comp. Mat.*, 42(26):2815–2827.

[Darcy, 1856] Darcy, H. (1856). Les fontaines publiques de la ville de dijon. *Dalmont, Paris*.

[Drummont and Tahir, 1984] Drummont, M. I. and Tahir, J. E. (1984). The permeability of fibrous porous media. *Int. J. Multiphase Flow*, 10(5):515–525.

[Dube et al., 2007] Dube, M., Daneault, C., Vuorinen, V., Alava, M., and Rost, M. (2007). Front roughening in three-dimensional imbibition. *Eur. Phys. J. B.*, 29(4):15–26.

[Dube et al., 2000] Dube, M., Rost, M., and Alava, M. (2000). Conserved dynamics and interface roughening in spontaneous imbibition: A critical overview. *Eur. Phys. J. B.*, 15:691–699.

[Dullien, 1979] Dullien, F. A. L. (1979). *Porous Media: Fluid Transport and Pore Structure*, pages 269–324. Academic Press Inc. San Diego.

[Dullien et al., 1977] Dullien, F. A. L., El-Sayed, M. S., and Batra, V. K. (1977). Rate of capillary rise in porous media with nonuniform pores. *J. Col. Interf. Sci.*, 60(3):497–506.

[Eker and Akin, 2006] Eker, E. and Akin, S. (2006). Lattice-boltzmann simulation of fluid flow in synthetic fractures. *Trans. Por. Media*, 65:363–384.

[El-Hosseiny, 1991] El-Hosseiny, F. (1991). Mathematical modelling of wet pressing of paper. *Nord. Pulp Paper Res. J.*, 6(1).

[Erickson et al., 2002] Erickson, D., Li, D., and Park, C. B. (2002). Numerical simulations of capillary-driven flows in nonuniform cross-sectional capillaries. *J. Col. Int. Sci.*, 250:422–430.

[Fabritius, 2007] Fabritius, T. (2007). *Optical method for liquid sorption measurements in paper*. Ph.D. Thesis, University of Oulu, Finland.

[Fourie et al., 2007] Fourie, W., Said, R., Young, P., and Barnes, D. L. (2007). The simulation of pore scale fluid flow with real world geometries obtained from x-ray computed tomography. *European COMSOL Multiphysics Conference, Boston. COMSOL inc.*

[Frishfelds et al., 2009] Frishfelds, V., Lundström, T. S., and Jakovics, A. (2009). Flow-induced deformation of non-crimp fabrics during composites manufacturing. *Proceedings in Interdisciplinary Transport Phenomena IV (ITP2009), Volterra, ITP-09-52*.

[Geindreau et al., 2009] Geindreau, C., Decain, M., and Bloch, J.-F. (2009). Private communication.

[Ginzburg, 2008] Ginzburg, I. (2008). Consistent lattice boltzmann schemes for the brinkman model of porous flow and finite chapman-enskog expansion. *Phys. Rev. E.*, 77(6):066704.

[Ginzburg and d'Humiéres, 2003] Ginzburg, I. and d'Humiéres, D. (2003). Multireflection boundary conditions for lattice boltzmann models. *Phys. Rev. E.*, 68(6):066614.

[Ginzburg et al., 2008] Ginzburg, I., Verhaeghe, F., and d'Humiéres, D. (2008). Two-relaxation-time lattice-boltzmann scheme: About parametrization,velocity, pressure and mixed boundary conditions. *Communications Comp. Phys.*, 32(2):427–478.

[Goel et al., 2006] Goel, A., Arns, C. H., Holmstad, R., Gregersen, O. W., Bauget, F., Averdunk, H., Sok, R. M., Sheppard, A. P., and Knackstedt, M. A. (2006). Analysis of the impact of papermaking variables on the structure and transport properties of paper samples by x-ray microtomography. *J. Pulp Paper Sci.*, 32(3):111–122.

[Goel et al., 2001] Goel, A., Tzanakakis, M., Huang, S., Ramaswamy, S., Choi, D., and Ramarao, B. (2001). Characterization of three-dimensional structure of paper using x-ray microtomography. *Tappi J.*, 84(5):72–80.

[Gonzalez and Woods, 2002] Gonzalez, R. and Woods, R. (2002). *Digital Image Processing*, pages 237–241. Prentice-Hall New-Jersey Inc.

[Grootenhuis, 1954] Grootenhuis, P. (1954). A correlation of the resistance to air flow of wire gauzes. *Proc. Institution Mech. Eng.*, 168:837–846.

[Happel, 1959] Happel, J. (1959). Viscous flow relative to arrays of cylinders. *AIChE*, 174.

[Hayashi, 2003] Hayashi, H. (2003). Lattice boltzmann method and its apllications to flow analysis in porous media. Res. Devel. Rev. 1, Toyota CRDL.

[Holmstad et al., 2003] Holmstad, R., Antonie, C., Nygard, P., and Helle, T. (2003). Quantification of the three-dimensional paper structure – methods and potential. *J. Pulp Paper Sci.*, 104(7):186–189.

[Holownia et al., 2008] Holownia, D., Kwiatkowska, I., and Hupka, J. (2008). An investigation on wetting of porous materials. *Physiochem. Prob. Mineral Proc.*, 42:251–261.

[Hyväluoma, 2009] Hyväluoma, J. (2009). A note on capillary invasion in non-uniform channels. *Int. J. Mod. Phys.*, 20(12):1903–1909.

[Hyväluoma et al., 2006] Hyväluoma, J., Raiskinmäki, P., Jäsberg, A., Koponen, A., Kataja, M., and Timonen, J. (2006). Simulation of liquid penetration in paper. *Phys. Rev. E.*, 73(3):036705.

[Jackson and James, 1986] Jackson, G. W. and James, D. F. (1986). The permeability of fibrous porous media. *Can. J. Chem. Eng.*, 64:364–373.

[Jaganathan et al., 2007] Jaganathan, S., Tafreshi, H. V., and Pourdeyhimi, B. (2007). A realistic approach for modeling permeability of fibrous media: 3-d imaging coupled with cfd simulation. *Chem. Eng. Sci.*, 63(1):224–252.

[Kataja et al., 1992] Kataja, M., Rybin, A., and Timonen, J. (1992). Permeability of highly compressible porous medium. *J. Appl. Phys.*, 72(1):1271.

[Keehm et al., 2006] Keehm, Y., Sternlof, K., and Mukerji, T. (2006). Computational estimation of compaction band permeability in sandstone. *Geosciences J.*, 10(4):499–505.

[Kerwald, 2004] Kerwald, D. (2004). Parallel lattice boltzmann simulation of complex flow. *NAFEMS Seminar: Simulation of Complex Flows (CFD)- Applications and Trends, Niedernhausen/Wiesbaden*, pages 1–23.

[Klinkenberg, 1941] Klinkenberg, L. J. (1941). The permeability of porous media to liquids and gases, drilling and production practice. *Am. Petrl. Inst.*, pages 200–213.

[Koponen et al., 1996] Koponen, A., Kataja, M., and Timonen, J. (1996). Tortuous flow in porous media. *Phys. Rev. Lett.*, 54(1):406–409.

[Kutay et al., 2006] Kutay, M. E., Aydilek, A. H., and Masad, E. (2006). Laboratory validation of lattice boltzmann method for modeling pore-scale flow in granular materials. *Computers and Geotechnics*, 33(8):381–395.

[Lenormand and Zarcone, 1984] Lenormand, R. and Zarcone, C. (1984). Role of roughness and edges during imbibition in square capillaries. *59th Annual Technical Conference of the Society of petroleum Engineers of AIME, Houston, Texas*, pages 1–15.

[Leskelä and Simula, 1998] Leskelä, M. and Simula, S. (1998). *Papermaking Science and Technology*, pages 284–317. Fapet Oy, Helsinki.

[Levitz, 2005] Levitz, P. (2005). Toolbox for 3d imaging and modeling of porous media: Relationship with transport properties. *Cement and Concrete Res.*, 37:351–359.

[Liakopoulos, 1965] Liakopoulos, A. C. (1965). Darcy's coefficient of permeability as symmetric tensor of second rank. *Hyrdl. Sci. J.*, 10(3):41–48.

[Lindsay and Brady, 1993a] Lindsay, J. D. and Brady, P. H. (1993a). Studies of anisotropic permeability with application to water removal in fibrous webs, part1. experimental methods, sheet anisotropy and relationships to freeness. *Tappi J.*, 76(9):119–127.

[Lindsay and Brady, 1993b] Lindsay, J. D. and Brady, P. H. (1993b). Studies of anisotropic permeability with application to water removal in fibrous webs, part2. relationships between water removal and permeability, and additional factors affecting permeability. *Tappi J.*, 76(11):167–174.

[Loosveld et al., 2002] Loosveld, H., Lafhaj, Z., and Skoczylas, F. (2002). Experimental study of gas and liquid permeability of a mortar. *Cement Concr. Res.*, 32:1357–1363.

[Lucas, 1918] Lucas, R. (1918). Über das zeitgesetz des kapillaren aufstiegs von flüssigkeiten. *Kolloid Z*, 23:15–22.

[Lundström et al., 2004] Lundström, T. S., Frishfelds, V., and Jakovics, A. (2004). A statistical approach to permeability of clustered fibre reinforcements. *J. Composite Mat.*, 38(13):1137–1149.

[Lundström et al., 2005] Lundström, T. S., Sundlöf, H., and Holmberg, J. (2005). Modeling of power-law fluid flow through fiber beds. *J. Composite Mat.*, 40(3):283–296.

[Manwart et al., 2002] Manwart, C., Aaltosalmi, U., Koponen, A., Hilfer, R., and Timonen, J. (2002). Lattice-boltzmann and finite-difference simulations for the permeability for three-dimensional porous media. *Phys. Rev. E.*, 66(1):016702.

[Martys and Hagedorn, 2002] Martys, N. S. and Hagedorn, J. G. (2002). Multiscale modeling of fluid transport in heterogeneous materials using discrete boltzmann methods. *J. Materials and Structures*, 35(10):650–659.

[Mélean et al., 2003] Mélean, Y., Broseta, D., Hasmy, A., and Blossey, R. (2003). Dispersion of imbibition fronts. *Europhys. Lett*, 62(4):505–513.

[Nordlund et al., 2005] Nordlund, M., Lundström, T., Frishfelds, V., and Jakovics, A. (2005). Permeability network model for non-crimp fabrics. *Composites Part A.*, 37:826–835.

[Nordlund et al., 2007] Nordlund, M., Lundström, T., Frishfelds, V., and Jakovics, A. (2007). Effect of multi-scale porosity in local permeability modelling of non-crimp fabrics. *Trans. Por. Media*, 72:109–124.

[Pan et al., 2006] Pan, C., Luo, L. S., and Miller, C. T. (2006). An evaluation of lattice boltzmann schemes for porous medium flow simulation. *Comp. Fluids*, 35(8-9):989–909.

[Pinker and Herbert, 1967] Pinker, R. A. and Herbert, M. V. (1967). Pressure loss associated with compressible flow through square-mesh wire gauzes. *J. Mech. Eng. Sci.*, 9(1):11–23.

[Ramaswamy et al., 2004] Ramaswamy, S., Gupta, M., Goel, A., Aaltosalmi, U., Kataja, M., Koponen, A., and Ramarao, B. V. (2004). The 3d structure of fabric and its relationship to liquid and vapor transport. *Coll. and Surf. A: Physiochem. Eng. Aspects*, 241:323–333.

[Rasi et al., 1999] Rasi, M., Koponen, A., Aaltosalmi, U., Timonen, J., Kataja, M., and Niskanen, K. J. (1999). Permeability of paper: Experiments and numerical simulations. *TAPPI, International Paper Physics Comference*, pages 297–306.

[Reverdy-Bruas et al., 2001] Reverdy-Bruas, N. R., Serra-Tosio, J.-M., Chave, Y., and Bloch, J.-F. (2001). Investigation of the transverse permeability of saturated paper sheets. *Drying tech.*, 19(10):2421–2433.

[Roberts et al., 2003] Roberts, R. J., Senden, T. J., Knackstedt, M. A., and Lyne, M. B. (2003). Spreading of aqueous liquids in unsized papers is by film flow. *J. Pulp Paper Sci.*, 29(4):123–131.

[Rolland du Roscoat et al., 2005] Rolland du Roscoat, S., Bloch, J.-F., and Thibault, X. (2005). Synchrotron radiation microtomography applied to paper investigation. *J. Phys. D: Appl. Phys.*, 38:A78–A84.

[Rolland du Roscoat et al., 2007] Rolland du Roscoat, S., Decain, M., Thibault, X., Geindreau, C., and Bloch, J. (2007). Estimation of microstructural properties from synchrotron x-ray microtomography and determination of the rev in paper materials. *Acta Mat.*, 55:2841–2850.

[Roux and Vincent, 1991] Roux, J. C. and Vincent, J. P. (1991). Vincent, a proposed model in the analysis of wet pressing. *Acta Geotechnica*, 74(2):189.

[Saar and Manga, 1999] Saar, M. O. and Manga, M. (1999). Permeability-porosity relationship in vesicular basalts. *Geophys. Res. Lett.*, 26(1):111–114.

[Samuelsen et al., 2001] Samuelsen, E. J., Houen, P. J., Gregersen, O. W., Helle, T., and Raven, C. (2001). Three dimensional imaging of paper by use of synchrotron x-ray microtomography. *J. Pulp Paper Sci.*, 27(2):50–53.

[Schlup et al., 2002] Schlup, J. R., Fan, L. T., and Johnson, R. A. (2002). Fluid flow through cattle hide: an experimental permeability study. *J. Mat. Sci.*, 37:795–799.

[Schoelkopf et al., 2002] Schoelkopf, J., Gane, P. A. C., Ridgway, C. J., and Matthews, G. P. (2002). "practical observation of deviation from Lucas-Washburn scaling in porous media". *Coll. Surf. A.*, 206:445–454.

[Senden et al., 2007] Senden, T. J., Bauer, A., Roberts, R. J., Salminen, L., Ettl, R., Champ, S., and Knackstedt, M. (2007). Experimental imaging of fluid penetration into papers. *61st Appita Annual Conference and Exhibition, Gold Coast, Australia 6-9 May, Proceedings, Carlton, Vic.: Appita Inc*, pages 149–153.

[Stock, 2009] Stock, S. R. (2009). *Micro Computed Tomography, Methodology and Applications*. CRC press Taylor and Francis Group, Boca Raton.

[Succi, 2001] Succi, S. (2001). *The Lattice Boltzmann Equation: For Fluid Dynamics and Beyond*. Oxford University press, Oxford.

[Succi et al., 1989] Succi, S., Foti, E., and Higuera, F. (1989). Three-dimensional flows in complex geometries with the lattice boltzmann method. *Europhys. Lett.*, 10(5):433–438.

[Tanikawa and Shimamoto, 2006] Tanikawa, W. and Shimamoto, T. (2006). Klinkenberg effect for gas permeability and its comparison to water permeability for fibrous sedimentary rocks. *Hydrol. Earth Syst. Sci. Discuss.*, 3(4):1315–1338.

[Taylor, 1997] Taylor, J. R. (1997). *An Introduction to Error Analysis. The study of uncertainties in physical measurements*. University Science Books, Sausalito.

[Thibault and Bloch, 2002] Thibault, X. and Bloch, J.-F. (2002). Structural analysis of x-ray microtomography of a strained nonwoven papermaker felt. *Textile Res. J.*, 72(6):480–485.

[Thibault and Bloch, 2008] Thibault, X. and Bloch, J.-F. (2008). Permeability measurements of strained fibrous networks. *Textile Res. J.*, 78(6):473–485.

[Torquato, 2001] Torquato, S. (2001). *Heterogeneous Materials, Microstructure and Macroscopic Properties*, pages 1–19. Springer-Verlag New York Inc.

[Turian and Kessler, 2000] Turian, R. M. and Kessler, F. D. (2000). Capillary flow in a noncircular tube. *AIChE J.*, 46(4):695–705.

[Verleye et al., 2007] Verleye, B., Croce, R., Griebel, M., Klitz, M., Lomov, S., Morren, G., Sol, H., Verpoest, I., and Roose, D. (2007). Permeability of textile reinforcements: Simulation, influence of shear and validation. *Composite Sci. Tech.*, 68(1):2804–2810.

[Verleye et al., 2005] Verleye, B., Klitz, M., Croce, R., Roose, D., Lomov, S., and Verpoest, I. (2005). Computation of permeability of textile reinforcements. *Proceedings in Scientific Computation IMACS 2005, Paris, France*.

[Versaevel et al., 2006] Versaevel, P., Colas, H., Rigaudeau, C., Noirot, R., Koltsakis, G. C., and Stamatelos, A. M. (2006). Some empirical observations on diesel particulate filter modeling and comparison between simulations and experiments. *Soc. Automotive Eng. Inc.*, 477:1–11.

[Vidal et al., 2008] Vidal, D., Ridgway, C., Pianet, G., Schoelkopf, J., Roy, R., and Bertrand, F. (2008). Effect of particle size distribution and packing compression on fluid permeability as predicted by lattice-boltzmann simulations. *Comp. Chem. Eng.*, 33(1):256–266.

[Vomhoff, 1998] Vomhoff, H. (1998). *Dynamic compressibility of water saturated fibre networks and influence of local sress variations in wet pressing*, pages 22–65. Ph.D. Thesis, Royal Institute of Technology, Stockholm, Sweden.

[Vomhoff, 2000] Vomhoff, H. (2000). On the in-plane permeability of water-saturated fibre webs. *Nord. Pulp Pap. Res J.*, 15(3):200–204.

[Vomhoff et al., 2000] Vomhoff, H., Martinez, D. M., and Norman, B. (2000). The transversal steady-state permeability of a fibre web compressed between rough permeable surfaces. *J. Pulp Paper Sci.*, 26(1):428–436.

[von Bahr et al., 2004] von Bahr, M., Seppänen, R., Tiberg, F., and Zhmud, B. (2004). Dynamic wetting of akd-sized papers. *J. Pulp Paper Sci.*, 30(3):74–81.

[Washburn, 1921a] Washburn, E. W. (1921a). Note on a method of determining the distribution of pore sizes in a porous material. *Proc. Natl. Acad. Sci.*, 7:115.

[Washburn, 1921b] Washburn, W. (1921b). The dynamics of capillary flow. *Phys. Rev.*, 17:273–283.

[Weighart, 1952] Weighart, K. E. G. (1952). On the resistance of screens. *Aeron. Quart.*, 4:186–192.

[White, 2003] White, F. M. (2003). *Fluid Mechanics*. McGraw-Hill, New York.

[White et al., 2006] White, J. A., Borja, I. R., and Fredrich, J. T. (2006). Calculating the effective permeability of sandstone with multiscale lattice-boltzmann/finite element simulations. *Acta Geotech.*, 33(1):195–209.

[Wiegmann, 2007] Wiegmann, A. (2007). Computation of the permeability of porous materials from their microstructure by fft-stokes. Report of the Fraunhofer ITWM 129, Fraunhofer Institute.

[Wu et al., 1998] Wu, Y.-S., Pruess, K., and Persoff, P. (1998). Gas flow in porous media with klinkenberg effects. *Trans. Por. media*, 32:117–137.

[Zhmud et al., 2000] Zhmud, B. V., Tiberg, F., and Hallstensson, K. (2000). Dynamics of capillary rise. *J. Coll. Int. Sci.*, 228:263–269.